Department Micro- and Nanosciences

Integration of GaAsP based III-V compound semiconductors to silicon technology

Henri Jussila

Aalto University

DOCTORAL DISSERTATIONS

Aalto University publication series
DOCTORAL DISSERTATIONS 135/2014

Integration of GaAsP based III-V compound semiconductors to silicon technology

Henri Jussila

A doctoral dissertation completed for the degree of Doctor of Science (Technology) to be defended, with the permission of the Aalto University School of Electrical Engineering, at a public examination held in the large seminar room at Micronova-building on the 26th of September 2014 at 12.

Aalto University
School of Electrical Engineering
Department of Micro- and Nanosciences

Supervising professor
Harri Lipsanen

Thesis advisors
Professor Markku Sopanen
Docent Teppo Huhtio

Preliminary examiners
Professor Olivier Durand, Université Européenne de Bretagne, France
Professor Doctor Wolfgang Stolz, Philipps-Universität Marburg, Germany

Opponent
Professor Robert Kudrawiec, Wroclaw University of Technology, Poland

Aalto University publication series
DOCTORAL DISSERTATIONS 135/2014

© Henri Jussila

ISBN 978-952-60-5848-1
ISBN 978-952-60-5849-8 (pdf)
ISSN-L 1799-4934
ISSN 1799-4934 (printed)
ISSN 1799-4942 (pdf)
http://urn.fi/URN:ISBN:978-952-60-5849-8

Unigrafia Oy
Helsinki 2014

Finland

A! Aalto University

Abstract

Aalto University, P.O. Box 11000, FI-00076 Aalto www.aalto.fi

Author	Henri Jussila
Name of the doctoral dissertation	Integration of GaAsP based III-V compound semiconductors to silicon technology
Publisher	School of Electrical Engineering
Unit	Department of Micro- and Nanosciences
Series	Aalto University publication series DOCTORAL DISSERTATIONS 135/2014
Field of research	Semiconductor materials
Manuscript submitted 10 April 2014	**Date of the defence** 26 September 2014
Permission to publish granted (date) 24 June 2014	**Language** English
☐ **Monograph**	☒ **Article dissertation (summary + original articles)**

Abstract

This thesis examines the integration of GaAsP based III-V compound semiconductors to silicon technology using two different concepts: the monolithic growth of GaP and the vapor-liguid-solid (VLS) growth of GaAs nanowires (NWs). Sample fabrication was performed by metalorganic vapor phase epitaxy. It was observed that the growth of GaP needs to be started at low temperatures to obtain a layer-by-layer growth mode. AFM examinations indicated that careful surface preparation prior to the growth is crucial. GaAs NWs were crystallized in the zinc-blende crystal structure and it was observed that the VLS growth method enables the fabrication of GaAs NWs on silicon and even on amorphous low-cost substrates.

The growth and characterization of Ga(As)PN alloys, with the composition nearly lattice-matched to silicon, was examined by various methods and it was observed that nitrogen incorporation complicates the growth process. Formation of a misfit dislocation network in the $GaP_{0.98}N_{0.02}$/GaP interface occurred when the film thickness was about 200 nm. The nitrogen incorporation efficiency was extremely low and it was observed that the amount of nitrogen related point defects increased with the nitrogen content. However, raman scattering and X-ray diffraction measurements implied that the nitrogen incorporation enables the fabrication of GaP based strain compensated structures on silicon substrates.

The effect of nitrogen incorporation on the energy band structure of GaAsPN was studied by photoluminescence (PL) and photoreflectance (PR) measurements. The different locations of PL and PR transitions suggested the PL signal to originate from the states related to nitrogen clusters. Furthermore, the conduction band splitting of GaAsPN alloys was observed by the PR measurements. Diodes fabricated from this material were chracterized to gather information from the absorption properties of the material. The photocurrent spectra revealed transitions from the split conduction band and the use of this type of structure in different solar cell devices was discussed.

The surface passivation of GaAs was studied fabricating a high-k metal insulator semiconductor capacitors from GaAs with an insulator stack comprised of an AlN surface passivation layer and a high-k HfO_2 layer. The Fermi level unpinning in the interface was shown by capacitance-voltage and current-voltage measurements.

Keywords semiconductor devices, MOVPE, silicon, gallium phosphide, integration, XRD		
ISBN (printed) 978-952-60-5848-1	**ISBN (pdf)** 978-952-60-5849-8	
ISSN-L 1799-4934	**ISSN (printed)** 1799-4934	**ISSN (pdf)** 1799-4942
Location of publisher Helsinki	**Location of printing** Helsinki	**Year** 2014
Pages 150	**urn** http://urn.fi/URN:ISBN:978-952-60-5849-8	

Aalto-yliopisto

Tiivistelmä

Aalto-yliopisto, PL 11000, 00076 Aalto www.aalto.fi

Tekijä
Henri Jussila

Väitöskirjan nimi
GaAsP-pohjaisten III-V yhdistepuolijohteiden integroiminen piiteknologiaan

Julkaisija Sähkötekniikan korkeakoulu

Yksikkö Mikro- ja Nanotekniikan laitos

Sarja Aalto University publication series DOCTORAL DISSERTATIONS 135/2014

Tutkimusala Puolijohdemateriaalit

Käsikirjoituksen pvm 10.04.2014 **Väitöspäivä** 26.09.2014

Julkaisuluvan myöntämispäivä 24.06.2014 **Kieli** Englanti

☐ **Monografia** ☒ **Yhdistelmäväitöskirja (yhteenveto-osa + erillisartikkelit)**

Tiivistelmä

Tämä väitöskirja tutkii GaAsP-pohjaisten III-V yhdistepuolijohteiden integroimista piiteknologiaan. Kaikki tutkitut näytteet valmistettiin metallo-orgaanisella kaasufaasiepitaksialla. Integroimismenetelminä käytettiin GaP-kiteen monoliittista valmistamista ja GaAs-nanolankojen valmistamista VLS-menetelmällä (*engl.* vapor-liquid-solid). Atomivoimamikroskooppikuvat valmistetuista GaP-kiteistä osoittivat, että piin pintakäsittely ennen kasvatusta on äärimmäisen tärkeää ja että kasvatus täytyy aloittaa matalassa lämpötilassa. Röntgendiffraktiomittaukset puolestaan osoittivat, että VLS-menetelmällä kasvatetut GaAs-nanolangat olivat kiteytyneet halutusti sinkkivälkehilaan.

GaAsPN-yhdisteen kasvatusta ja erilaisia ominaisuuksia tutkittiin monella eri menetelmällä. Näissä tutkimuksissa huomattiin, että typen lisääminen kiteeseen aiheuttaa monia ongelmia. Epäsopudislokaatioverkon (*engl.* misfit dislocation network) huomattiin syntyvän $GaP_{0.98}N_{0.02}$/GaP-rajapintaan kerrospaksuuden ylittäessä 200 nm. Typen substituution kiteeseen havaittiin heikkenevän ja lopulta häviävän typpipitoisuuden kasvaessa. Raman- ja XRD-mittaukset kuitenkin viittasivat siihen, että typen lisääminen GaP-kiteeseen pienentää hilaepäsovusta syntyvää jännitystä, jos GaPN-kide on kasvatettu piin päälle.

GaAsPN-energiavyörakennetta tutkittiin fotoluminesenssi- ja fotoreflektanssimittausmenetelmillä. GaPN:sta fotoreflektanssilla mitatun transition huomattiin sijaitsevan eri paikassa kuin missä sen fotoluminesenssimittauksen perusteella uskottiin sijaitsevan. Tämä selitettiin sillä, että fotoluminesenssin havaitsema suora transitio tapahtui monimutkaisten typpikonfiguraatioiden muodostamista energiatiloista jotka sijaitsivat fotoreflektanssin havaitseman transition alapuolella. Fotoreflektanssimittaus havaitsi GaAsPN:n johtavuusvyön jakaantumisen. Tätä materiaalia käytettiin aurinkokennojen valmistukseen ja tämän materiaalin ominaisuuksien hyötykäyttöä erilaisissa aurinkokennosovelluksissa pohdittiin.

GaAs:n pintapassivointia tutkittiin valmistamalla metalli-eriste-puolijohdekondensattoreita. Komponenttien eristekerros valmistettiin suuren dielektrisyysvakion omaavasta HfO_2:sta ja 2 nm paksusta AlN:stä valmistetusta passivointikerroksesta käyttäen ALD-valmistusmenetelmää (*engl.* atomic layer deposition). Kapasitanssi-jännite ja virta-jännitemittaustulokset viittasivat siihen, että yleisesti havaittua *Fermi level pinning* -ilmiö ei ilmennyt komponentin toiminnassa.

Avainsanat puolijohdekomponentit, MOVPE, pii, gallium fosfidi, integraatio, XRD

ISBN (painettu) 978-952-60-5848-1 **ISBN (pdf)** 978-952-60-5849-8

ISSN-L 1799-4934 **ISSN (painettu)** 1799-4934 **ISSN (pdf)** 1799-4942

Julkaisupaikka Helsinki **Painopaikka** Helsinki **Vuosi** 2014

Sivumäärä 150 **urn** http://urn.fi/URN:ISBN:978-952-60-5849-8

Preface

The work presented in this thesis was carried out at the Department of Micro- and Nanosciences, School of Electrical Engineering, Aalto University, between 2010 and 2014. However, my life in this Department started as early as Summer 2006 when I got a summer trainee position. At that time, I was a first year student and pretty much only understood that the phrase *nano* refers to something really small. About semiconductors, I most likely had no clue what they were and how the modern society utilizes them. Thus, after those days I have learned a lot and am grateful to many people without whom this thesis would have never become ready.

Firstly, I want to express my sincere and deepest gratitude to Professor Harri Lipsanen for supervising this thesis and for all the valuable advice and suggestions he has given me. I want to thank Professor Markku Sopanen, thesis advisor and also supervisor of this thesis, for all the help I have received. I am also grateful to him for the opportunity to work in his group and for being able to examine this interesting topic. I would like to thank Docent Teppo Huhtio for all the fruitful discussions relating to this work. Professor Turkka Tuomi is deeply acknowledged for all the help and for numerous interesting discussions we have had in Micronova and also in XRD topography beamlines.

I am also in dept to all my colleagues who have always provided the help I have needed and made it for me fun to come to work every day. Most likely some names are missing but at least I need to express my deepest gratitude to M.Sc Päivi Mattila, Dr. Marco Mattila, M.Sc Sakari Sintonen, Jori Lemettinen, Dr. Sami Suihkonen, Dr. Lasse Karvonen, Dr. Tapani Alasaarela, M.Sc Lauri Riuttanen, Dr. Nagarajan Subramaniyam, Dr. Veer Dhaka, M.Sc Tuomas Haggren, M.Sc Alex Perros, M.Sc Anders Olsson, M.Sc Olli Svensk, Juha-Matti Tilli and Professor Seppo Honkanen. I have learned a lot from you all!

Finally, I want to express my gratitude to my parents Kari and Helena, and my brother Tomi for all their love and support.

Espoo, September 4, 2014,

Henri Jussila

Contents

Preface i

Contents iii

List of Publications v

Author's Contribution vii

1. Introduction 1

2. Properties of III-V compound semiconductors and silicon 5

2.1 Crystal structure 5

2.2 Energy band structure: electrical and optical properties of semiconductors 7

3. Metalorganic vapor phase epitaxy 11

4. Characterization methods 15

4.1 Atomic force microscopy 15

4.2 X-ray diffraction 16

4.2.1 Bragg's law and its utilization in XRD measurements 17

4.2.2 Transverse scan measurements 18

4.2.3 Synchrotron XRD topography 18

4.3 Rutherford backscattering spectroscopy 19

4.4 Optical spectroscopy 20

4.4.1 Photoluminescence 20

4.4.2 Photoreflectance 21

4.5 Capacitance voltage characterization and the Terman method 22

5. Integration of III-V compounds on silicon: monolithic growth of GaP layers and vapor-liquid-solid growth of GaAs nanowires 25

5.1 Common integration approaches 25
5.2 Monolithic integration of GaP on silicon 28
5.2.1 AFM studies of GaP layers on silicon 28
5.2.2 Structural study of thin GaP layers on silicon by transverse scan analysis 31
5.3 GaAs nanowires on silicon and low-cost glass substrates . . 34

6. Characterization of Ga(As)PN materials 37
6.1 Structural properties of GaPN alloys 38
6.1.1 Strain relaxation in GaPN layers on GaP substrates . 38
6.1.2 Nitrogen substitutionality in GaPN layers 39
6.1.3 Strain compensation of GaPN layers on silicon 42
6.2 Energy band structure of Ga(As)PN 43

7. Properties of the fabricated semiconductor devices that could be integrated on silicon substrate 49
7.1 Use of GaAsPN in silicon based solar cells and intermediate band solar cells 49
7.2 GaAs MIS structures 53

8. Summary 57

Bibliography 61

Publications 69

List of Publications

This thesis consists of an overview and of the following publications which are referred to in the text by their Roman numerals.

I H. Jussila, S. Nagarajan, T. Huhtio, H. Lipsanen, T. O. Tuomi, and M. Sopanen. Structural study of GaP layers on misoriented silicon (001) substrates by transverse scan analysis. *Journal of Applied Physics*, **111**, 043518, 6p., 2012.

II H. Jussila, S. Nagarajan, P. Mattila, J. Riikonen, T. Huhtio, M. Sopanen, and H. Lipsanen. Growth and characterization of GaP layers on silicon substrates by metal-organic vapour phase epitaxy. *Physica Status Solidi C*, **9**, 7, 1607-1609, 2012.

III V. Dhaka, T. Haggren, H. Jussila, H. Jiang, E. Kauppinen, T. Huhtio, M. Sopanen, and H. Lipsanen. High Quality GaAs Nanowires Grown on Glass Substrates. *Nano Letters*, **12**, 4, 1912-1918, 2012.

IV T. Haggren, A. Perros, V. Dhaka, T. Huhtio, H. Jussila, H. Jiang, M. Ruoho, E. Kauppinen, and H. Lipsanen. GaAs Nanowires grown on Al doped ZnO buffer layers. *Journal of Applied Physics*, **114**, 084309, 7p., 2013.

V H. Jussila, S. Nagarajan, S. Sintonen, S. Suihkonen, A. Lankinen, T. Huhtio, C. Paulmann, H. Lipsanen, T. O. Tuomi, and M. Sopanen. Evaluation of critical thickness of $GaP_{0.98}N_{0.02}$ layer on GaP substrate by synchrotron X-ray diffraction topography. *Thin Solid Films*, **531**, 680-

684, 2013.

VI H. Jussila, K. M. Yu, J. Kujala, F. Tuomisto, S. Nagarajan, J. Lemettinen, T. Huhtio, T.O. Tuomi, H. Lipsanen and M. Sopanen. Substitutionality of nitrogen atoms and formation of nitrogen complexes and point defects in GaPN alloys. *Journal of Physics D: Applied Physics*, **47**, 075106, 6p., 2014.

VII S. Nagarajan, H. Jussila, J. Lemettinen, K. Banerjee, M. Sopanen, and H. Lipsanen. Strain-compensated GaPN/GaP heterostructure on silicon (100) substrates for intermediate band solar cells. *Journal of Physics D: Applied Physics*, **46**, 165103, 6p., 2013.

VIII H. Jussila, P. Mattila, J. Oksanen, A. Perros, J. Riikonen, M. Bosund, A. Varpula, T. Huhtio, H. Lipsanen, and M. Sopanen. High-k GaAs metal insulator semiconductor capacitors passivated by ex-situ plasma-enhanced atomic layer deposited AlN for Fermi-level unpinning. *Applied Physics Letters*, **100**, 071606, 4p., 2012.

Author's Contribution

Publication I: "Structural study of GaP layers on misoriented silicon (001) substrates by transverse scan analysis"

The author fabricated the samples, did the experiments, analysed the results with the help of the other co-authors, and wrote the first manuscript.

Publication II: "Growth and characterization of GaP layers on silicon substrates by metal-organic vapour phase epitaxy"

The author fabricated the samples, did the experiments, analysed the results with the help of the other co-authors, and wrote the first manuscript.

Publication III: "High Quality GaAs Nanowires Grown on Glass Substrates"

The author performed the XRD experiments and helped to prepare the manuscript.

Publication IV: "GaAs Nanowires grown on Al doped ZnO buffer layers"

The author performed the XRD experiments and helped to prepare the manuscript.

Publication V: "Evaluation of critical thickness of $GaP_{0.98}N_{0.02}$ layer on GaP substrate by synchrotron X-ray diffraction topography"

The author fabricated the samples, did the XRD topography experiments with co-author S. Sintonen, analysed the results and wrote the first manuscript.

Publication VI: "Substitutionality of nitrogen atoms and formation of nitrogen complexes and point defects in GaPN alloys"

The author fabricated the samples, did the photoluminescence measurements and wrote the first manuscript.

Publication VII: "Strain-compensated GaPN/GaP heterostructure on silicon (100) substrates for intermediate band solar cells"

The author fabricated the samples, did the photoreflectance measurements and helped to prepare the manuscript.

Publication VIII: "High-k GaAs metal insulator semiconductor capacitors passivated by ex-situ plasma-enhanced atomic layer deposited AlN for Fermi-level unpinning"

Relating to the sample fabrication, the author did the MOVPE growth and the metal evaporation. The simulations and the experiments were performed by the author with co-authors J. Oksanen and P. Mattila, respectively. The author analysed the experimental results and wrote the first manuscript.

List of Abbreviations

AFM	Atomic force microscopy
ALD	Atomic layer deposition
AlN	Aluminum nitride
APD	Antiphase domain
AZO	Aluminum doped zinc oxide
BAC	Band anticrossing
CMOS	Complementary metal oxide semiconductor
CV	Capacitance voltage measurement
DMHy	Dimethyl hydratzine
ELOG	Epitaxial lateral overgrowth
GaAs	Gallium arsenide
GaN	Gallium nitride
GaP	Gallium phosphide
HfO_2	Hafnium oxide
IB	Integral breadth
IBSC	Intermediate band solar cell
IC	Integrated circuit
ITRS	International technology roadmap for semiconductors
LED	Light emitting diode
MOSFET	Metal oxide semiconductor field effect transistor
MOVPE	Metalorganic vapor phase epitaxy
NRA	Nuclear reaction analysis
PL	Photoluminescence
PR	Photoreflectance
QF	Quality factor
RBS	Rutherford backscattering

TBP	Tertiarybutyl phosphine
TBAs	Tertiarybutyl arsine
TMGa	Trimethyl gallium
VLS	Vapor liquid solid
XRD	X-ray diffraction

List of Symbols

a	Lattice constant
d	Distance between diffracting crystal planes
E	Energy
f_{sub}	Substitutional nitrogen fraction
f_I	Interstitial nitrogen fraction
f_{rand}	Random nitrogen fraction
$\boldsymbol{k}$	Wavevector
S	Diffraction vector
2θ	XRD goniometer angle between the diffracted and transmitted X-ray beam
λ	Wavelength
ϕ	Azimuth angle of the XRD goniometer
ψ	XRD goniometer angle tilting the normal of the sample
ω	XRD goniometer angle between the sample surface and the incident X-ray beam

1. Introduction

In 1931 Wolfgang Pauli, a later Nobel Laureate in physics, has been told to express an opinion: *one should not work on semiconductors, that is a filthy mess; who knows whether any semiconductors exist*. Pauli's comment describes well how quickly the world did change in the twentieth century. At the moment, the properties of semiconductors are well-known and it is practically impossible to find any electronic device that is not utilizing semiconductor materials in its operation. In fact, semiconductor materials have enabled the building of the modern information society.

The most commonly used semiconductor material is silicon. The advantages of silicon are, in addition to the general property of semiconductors to control the conductivity type of the material locally by doping, that large high quality substrates can be fabricated, silicon is cheaply available around the world and that the interface between silicon and silicon oxide is almost perfect. The high quality silicon/silicon oxide interface enables the fabrication of metal-oxide-semiconductor field effect transistors (MOSFET) that do all the operations in complementary metal oxide semiconductor (CMOS) computer chips. The exponential increase in the performance of computers has resulted from the enhanced processing methods that have enabled the fabrication of a larger number of transistors in an increasingly smaller volume of a computer chip. In fact, during the last 50 years this progress has followed the Moore's law which states that the number of components in a computer chip doubles every two years [1]. However, in order to maintain the exponential improvement rate new methods are required because with this rate the size of a single transistor approaches the size of an atom in the next decades.

At the moment, the scaling has already proceeded so far that the silicon oxide gate dielectrics would be required to be sub-nanometer thick which causes large leakage currents and prevents the operation of traditional

CMOS circuits. This problem was already solved in the 45 nm transistor node by replacing the silicon oxide with high-k dielectrics that enable the same operation with thicker gate dielectrics. In addition, the performance of transistors has also been enhanced in sub 130 nm transistor nodes by strain engineering depositing a germanium layer on silicon wafers. The channel mobility increases with the strain in CMOS substrates, and thus, enhances the device performance. This all exemplifies that new component designs, in which materials different than silicon are integrated into silicon chips, belong to the future of semiconductor industry.

Today, III-V compound semiconductors are mainly used in optoelectronic components fabricated from InGaAs, GaAs, and InP especially for telecommunication and the GaN based LEDs and laser diodes used in household lighting and *Blu-ray* mediaplayers. In 2012, the global sales of all III-V compound semiconductor components totaled 27 billion dollars. The usage of these materials in optoelectronic components originates from their energy band structure which enables the fabrication of efficiently operating luminescent components. In addition to the direct band gap, however, III-V compound semiconductors have many other advantages over silicon. For instance, the electron mobilities of these materials can be as much as 50 times larger than the electron mobility of silicon. Furthermore, the electronic band structure can be engineered easily by simply alloying the materials with other group III or group V elements.

Integration of III-V compound semiconductors on silicon would allow semiconductor industry to include the properties of III-V compound semiconductor materials that silicon does not possess in the component design. The device concepts that have received the most attention include CMOS compatible lasers that could be used in on-chip and chip-to-chip communication [2, 3], high mobility transistors and silicon based multijunction solar cells [4, 5]. For instance, the utilization of high-mobility III-V compound semiconductors in IC technology was recently included in the international technology roadmap for semiconductors [6]. The idea to integrate III-V compound semiconductors to silicon technology is old but has not yet become a standard technique in industry. The direct epitaxy of III-V compounds on silicon (*i.e.*, the monolithic growth) has many times been ruled to be too difficult. However, quite recently the monolithic growth of high-quality GaP on silicon was demonstrated [7–9] and this approach has been used to fabricate the first monolithically integrated electrically pumped high quality laser diodes on silicon substrates [10]. In addition

to the GaP concept, also the metamorphic growth of GaSb has received a lot of attention lately and been used to fabricate monolithically integrated laser diodes on silicon[11].

In this thesis, GaAsP based materials that could be integrated to silicon substrates are examined. The thesis is organized in the following way. Chapter 2 briefly reviews the general properties of semiconductors and provides a theoretical backround for the reader. The most important experimental methods are reviewed in Chapters 3 and 4. Chapter 5, on the other hand, discusses integration of III-V compound materials on silicon substrates. Firstly, the most common integration approaches are listed. Then, the discussion follows the work performed to GaP layers grown monolithically on silicon substrates by metalorganic vapor phase epitaxy. In addition, the work relating to the growth of GaAs nanowires on silicon and also on other low-cost substrates is briefly discussed. Chapter 6 focuses on the growth and characterization of Ga(As)PN materials. This compound semiconductor alloy is interesting because it enables the strain compensation on silicon in addition to the possibility to engineer the energy band structure of the material. Lastly, Chapter 7 presents the work relating to the fabrication and characterization of III-V based solar cell and MOSFET devices.

2. Properties of III-V compound semiconductors and silicon

This chapter reviews theory relating to the crystal structure and the electronic band structure of semiconductor materials. Typically, semiconductor devices are fabricated from semiconductor crystals, *i.e.*, materials in which the atoms are organized at locations that can be constructed by placing multiple unit cells, which operate as crystal building blocks, next to each other. Firstly, the crystal structure of semiconductors and some typical imperfections existing in real crystals are reviewed. Then, the electrical and optical properties of III-V compound semiconductors and silicon are discussed with the help of the energy band structure.

2.1 Crystal structure

III-V compound semiconductors and silicon typically crystallize in zinc-blende and diamond crystal structures, respectively. The unit cell of the zinc-blende crystal structure is shown schematically in Fig. 2.1. The zinc blende crystal is comprised of two face centered cubic lattices with one sublattice shifted by a quarter of the diagonal along the diagonal direction with respect to the other sublattice. The diamond crystal structure is similar to that of the zinc-blende crystal structure with the exception that atoms in the diamond structure are the same in both sublattices.

Real crystals are never perfect. Some imperfections always exist in the ordering of atoms changing the electronic properties of the materials and degrading the performance of semiconductor devices fabricated from these crystals. Crystal imperfections can be divided into two subcategories: point defects, and extended defects. Some of these defects are illustrated schematically in Fig. 2.2. Point defects comprise of the defects in which the crystal imperfection is local (*i.e.*, a few nanometers). Typical point defects include vacancies, interstitials, and defect complexes. In a

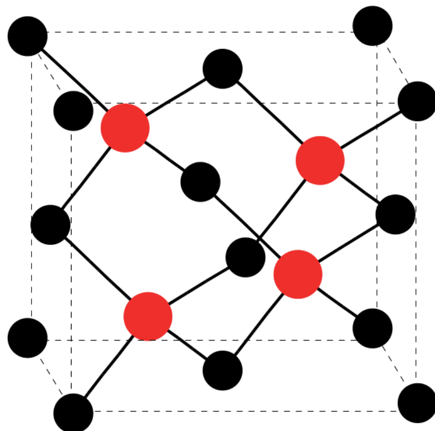

Figure 2.1. Unit cell of the zincblende crystal lattice is comprised of two face centered cubic lattices one of which is occupied by group V atoms (black circles) and the other by group III atoms (red circles). Bonds between the atoms are marked with black lines. The dashed line illustrates schematically the outer bound of the unit cell. The length of the edge is called the lattice constant of the crystal.

vacancy type defect, an atom is missing from the crystal lattice and the lattice site is unoccupied. In an interstitial, an extra atom locates at a position not belonging to the lattice. Defect complexes, on the other hand, are defects in which the crystal defect forms between different kinds of clusters of vacancies, interstitials and impurities.

Extended defects are the other type of crystalline defects in which the crystal imperfection exists in a larger volume of the crystal. Stacking faults, dislocations, and antiphase domains exemplify this type of crystal defects. For instance, a dislocation can be a line of atoms misaligned with respect to the other part of the crystal. Stacking faults, on the other hand, are crystal planes that change the convenient stacking order of the crystal. Antiphase domains which can be encountered when III-V compound semiconductors are grown on silicon exist in crystals comprised of two different atoms. Antiphase domains are regions in which every individual plane of atoms is comprised of the other of the two atoms than the rest of the crystal (see the horizontal (001) planes of Fig. 2.2). As a result of this, the edges of the antiphase domains, *i.e.*, antiphase boundaries, are comprised of the bonds between the same atoms (*e.g*, Ga-Ga or P-P bonds in gallium phosphide).

Many reasons exist for the formation of crystal defects. For instance, semiconductor crystals are typically fabricated at high temperatures forcing the atoms to diffuse during fabrication. As a result of diffusion, atoms

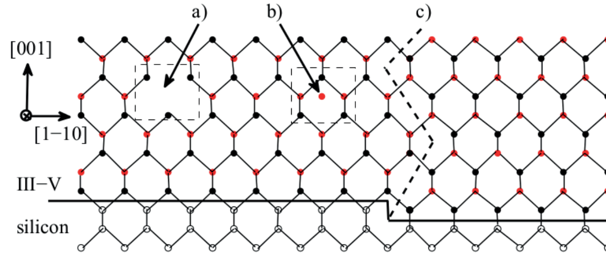

Figure 2.2. Schematical illustration of crystal imperfections in the zinc-blende GaP layer on silicon viewed along the [-1-10] direction: (a) a Ga-vacancy, (b) a Ga-interstitial atom, and (c) an antiphase boundary. The thick line represents the interface between the silicon and the GaP layer.

sometimes locate at non-optimal positions which may lead to formation of point defects. Dislocation type defects can form to relieve strain between the two materials with different unit cell sizes and may be even centimeters long. However, whatever is the reason behind the formation of a certain type of a crystal defect it is important to reduce their density. Crystal defects can be charged or contain atypical bonds, and thus, affect the electrical properties of the material. In the worst case, crystal defects may prevent the operation of the device, *e.g.*, by lowering the breakdown voltage of a diode or by acting as conductive channels.

2.2 Energy band structure: electrical and optical properties of semiconductors

The energy bands of semiconductor crystals originate from all the allowed energy/wavevector -pairs of charge carriers that satisfy the time-independent Schrödinger equation. Typically, the energy band structure of semiconductors is drawn for the two most important energy bands: the conduction band and the valence band, which are often used to explain the electrical and optical properties of semiconductors. The bands are defined in such a way that at the temperature of 0 K the conduction band is the lowest (in energy) completely empty energy band and the valence band is the highest completely filled band. The energy difference between the two extrema of these bands is called the band gap energy. The energy band structures of silicon, gallium phosphide and gallium arsenide are drawn schematically in Fig. 2.3.

For a material to conduct electricity, a partially empty energy band is required. Charge carriers are fermions, and as a result, cannot occupy

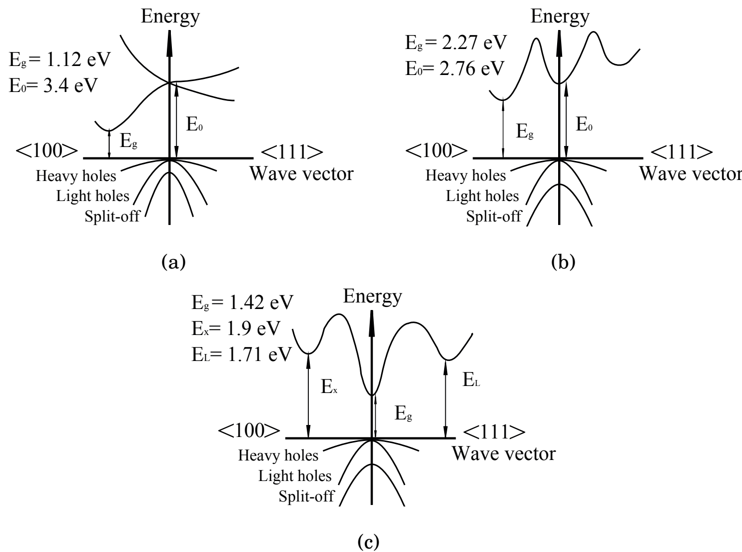

Figure 2.3. Energy band structures of (a) silicon, (b) gallium phosphide, and (c) gallium arsenide show different transition energies between the valence band (comprised of heavy hole, light hole and split-off bands) and the conduction band. GaP and silicon are indirect gap semiconductors due to the location of the conduction band minimum at the X-valley.

the same state that another charge carrier already occupies. Therefore, the number of charge carriers in any given state is affected by whether the state is already occupied or if an energy state with that energy is allowed, *i.e.*, is a solution of the Schrödinger equation. A density of states function is used for this purpose. In addition, the probability of any energy state to be occupied by a charge carrier follows the Fermi-Dirac statistics. As a result of the above, perfect semiconductors do not conduct electricity at 0 K temperature. However, at higher temperatures, the conduction and the valence bands are typically occupied by charge carriers due to the Fermi-Dirac distribution, and thus, the electrical conductivity increases with temperature.

The location of the Fermi energy can be engineered and the electrical conductivity of semiconductors increased by doping. Doping means intentional introduction of foreign atoms into the semiconductor crystal. Dopant atoms have typically one extra or missing electron in the outest electron shell compared to the atoms of the host material. Thus, group III and group V atoms operate as dopants for Si (and reversibly Si atoms operate as dopants for III-V compound semiconductors). Dopant atoms enable the fabrication of semiconductor layers that conduct electricity even at low temperatures. However, a drawback of doping is that the dopants

decrease the mobility of charge carriers due to increased scattering. The mobility is an important measure describing the capacity of the material to respond to the electric field. All intrinsic scattering processes, such as phonon scattering, that charge carriers experience decrease the mobility of semiconductors. In addition, the mobility decreases also due to scattering caused by a larger density of defects.

The recombination and excitation processes of charge carriers can also be explained with the energy band structure. General rule for these processes is the conservation laws of energy and momentum (*i.e.*, wavevector). Thus, in order for an electron to be excited or recombined from one band to the other, absorption or emission of energy is required. Energy does not disappear but instead transforms to other forms in these processes. Typically, photons and phonons are involved in recombination and excitation processes of semiconductor materials. The property of semiconductors that is important for optoelectronic devices is whether the band gap of the material is direct or indirect. In direct gap semiconductors like GaAs, the minimum of the conduction band and the maximum of the valence band locates at the same wavevector, $\mathbf{k}$, value (see Fig. 2.3). In indirect gap semiconductors like GaP and silicon, the extreme values of the bands are at different positions of the $\mathbf{k}$-space. Therefore, due to the nearly zero wavevector of photons the recombination process in which a photon is emitted is significantly more probable in direct gap semiconductors than in indirect gap materials. As a result, optoelectronic light emitting semiconductor components such as LEDs or lasers are fabricated from direct gap semiconductors. The emission wavelength of these devices is usually defined by the band gap of the material.

Table 2.1 lists the band gap energies and the charge carrier mobilities of different semiconductor materials mentioned in this thesis. It can be observed that the electron mobilities of many III/V compound semiconductors outperform silicon (*e.g.*, InSb by a factor of 55). However, the hole mobilities of III/V compound semiconductors are comparable to silicon. Germanium possesses the highest mobility for holes. The band gaps of III-V compound semiconductors are between 6 eV and 0.17 eV. Thus, III-V compound semiconductor devices can emit and absorb radiation between ultraviolet and infrared wavelengths.

Table 2.1. Summary of crystal structures, band gaps and mobilities of various semiconductor materials at room temperature. Mobilities are given in units of $\frac{cm^2}{Vs}$. The lattice constant values for the wurtzite crystal differ between the a- and c-direction of the crystal.

	Lattice constant	Crystal structure	Band gap	Energy gap	Electron mobility	Hole mobility
Si	5.43 Å	Diamond	1.12 eV	indirect	1400	450
GaP	5.45 Å	Zinc-Blende	2.26 eV	indirect	250	150
GaAs	5.65 Å	Zinc-Blende	1.42 eV	direct	8500	400
GaN	4.52 Å	Zinc-Blende	3.2 eV	direct	1000	350
GaN	a=3.18 Å c=5.19 Å	Wurtzite	3.39 eV	direct	1000	200
AlN	a=3.11 Å c=4.98 Å	Wurtzite	6.2 eV	direct	300	14
Ge	5.66 Å	Diamond	0.66 eV	indirect	3900	1900
InSb	6.45 Å	Zinc-Blende	0.17 eV	direct	77000	850

3. Metalorganic vapor phase epitaxy

Metalorganic vapor phase epitaxy (MOVPE) and molecular beam epitaxy are standard growth methods used in the industry for fabrication of III-V compound semiconductor materials. This chapter explains briefly the theory related to the MOVPE fabrication method and presents the apparatus used for fabrication of the samples discussed in this thesis.

All of the samples grown for this thesis were fabricated using the MOVPE system manufactured by Thomas Swan & Co. Ltd. The schematic of the MOVPE tool, which is located in the Micronova building, is presented in Fig. 3.1. The conditions inside the reactor during growth are defined with the growth recipe program. The gas system, which connects the organometallic source materials through the reactor to the exhaust, is composed of gas lines, mass flow controllers (MFC), valves, and bubblers. Organometallic source materials; carbon compounds comprised of carbon, hydrogen, and group III or group V atoms, are held inside bubblers located in liquid baths. The temperature of the baths can be controlled between -20°C and 30°C, so that a suitable vapor pressure of the source material can be chosen. When the carrier gas flows through the bubbler, the carrier gas becames saturated with the precursor and carries the source materials to a heated quartz-glass reactor where the growth occurs. The fluxes of the different gas flows are controlled by MFCs.

The substrate is placed on the top of a graphite susceptor inside the reactor. The susceptor can be heated up to 850°C by an infrared lamp, which is located under the susceptor. The temperature of the susceptor is measured by a thermocouple element inside the susceptor. Therefore, the real temperature of the substrate surface is actually lower than the thermocouple reading due to the cooling effect of the flowing gas. All growth temperatures mentioned later in this thesis are thermocouple readings. The thermocouple is protected with a quartz-glass tube.

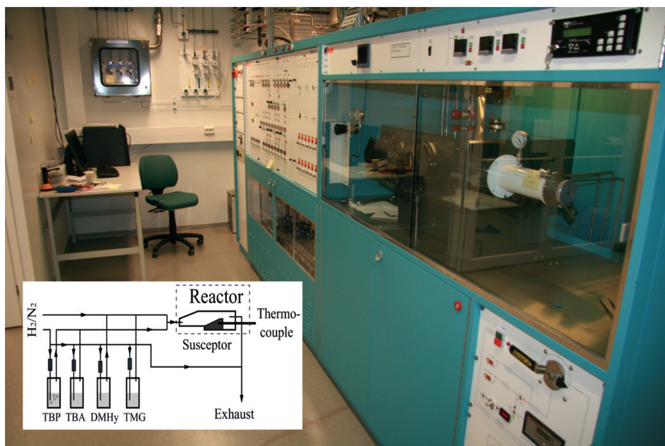

Figure 3.1. MOVPE apparatus and a schematic of its gas system. Gas fluxes are controlled by MFCs which are illustrated by gray boxes. The bubblers locate inside liquid baths.

Organometallic source materials decompose to group III and group V atoms due to the increased temperature inside the reactor. This decomposition reaction is called pyrolysis and is an extremely complex set of chemical reactions. However, for the crystal grower it is sufficient to know at which temperature the pyrolysis occurs. This temperature is typically between 400°C and 550°C and sets a lower boundary for the growth temperature. After decomposition, group III and group V atoms diffuse in the gas phase and can eventually be adsorbed on the sample surface. On the surface of the sample, adatoms can experience diffusion before they are bound at some location. In addition, the adatoms that are already located on the surface can be desorbed. Desorption rate is larger at higher temperatures. Usually, the sample surface is protected from desorption by supplying group V atoms with a high rate, causing that if any group V atom is desorbed it is likely that a new group V atom replaces it. Thus, the V/III ratios which describe the ratio between the gas fluxes of group III and group V sources are typically high during the growth. A sideproduct of the high V/III ratio is that the growth rate of the film can be defined with the flow of the group III source.

During growth all of the aforementioned processes that adatoms experience occur simultaneously and are driven by thermodynamics, reaction kinetics in the gas phase and the attempt of the film to minimize its total energy. Metalorganic vapor phase epitaxy, like the name states, is an epitaxial method meaning that the grown layer attempts to copy the crystal structure of the layer below it. Hence, differences in crystal structure,

crystal polarity, thermal expansion coefficient, surface energy, *etc.*, all affect the outcome of the growth. In general, thin films will form via three different growth modes. In Frank-Van der Merwe (FM) growth mode, the growth occurs two-dimensionally one atomic layer at a time. The growth mode where the adsorbed atoms form clusters and three-dimensional islands but do not wet the surface is called Volmer-Weber. Intermediate for the two growth modes is the Stranski-Krastanow growth mode in which the adatoms first form a smooth two-dimensional layer but then when a certain critical thickness is exceeded start to form islands. For the growth of thin films, the FM growth mode is desired but not always the preferable growth mechanism. In this thesis, the selection of the growth mode was affected by altering the growth parameters and is explained in more detail in chapter 5.

4. Characterization methods

This chapter reviews some of the experimental characterization methods used in this thesis. In addition to the methods described below, also scanning electron microscopy (SEM), transmission electron microscopy (TEM), X-ray reflection, current-voltage (IV), Raman spectroscopy, photocurrent spectroscopy, Hall measurement and positron annihilation spectroscopy were used in the publications.

4.1 Atomic force microscopy

Atomic force microscopy (AFM) is a characterization method used to measure the morphology of the sample surface. AFM belongs to the family of scanning probe microscopy. The vertical resolution of AFM is less than 1 nm. An AFM apparatus is composed of a cantilever and a tip, a laser system, a photodetector, feedback electronics, and a piezoelectric sample holder. The operation principle of AFM is based on the atomic interactions between the tip and the surface of the sample. Different operating modes of AFM utilize different interactions. All the images presented in this thesis were taken in semicontact mode, *i.e.*, utilizing the fact that the resonance frequency of the AFM tip depends on the distance between the sample surface and the tip. This distance is typically a few nanometers during the imaging. The information from the resonance is gathered from the back reflection of the laser beam from the back of the cantilever with the photodetector. The piezoelectric sample holder allows the position of the sample to be controlled with nanometer precision and imaging is performed by scanning the sample surface. The maximum scan size of the used NTegra Aura AFM is 13×13 μm^2. While scanning, the distance between the tip and the sample surface depends on the morphology of the sample and, thus, changes constantly. AFM attempts to maintain the dis-

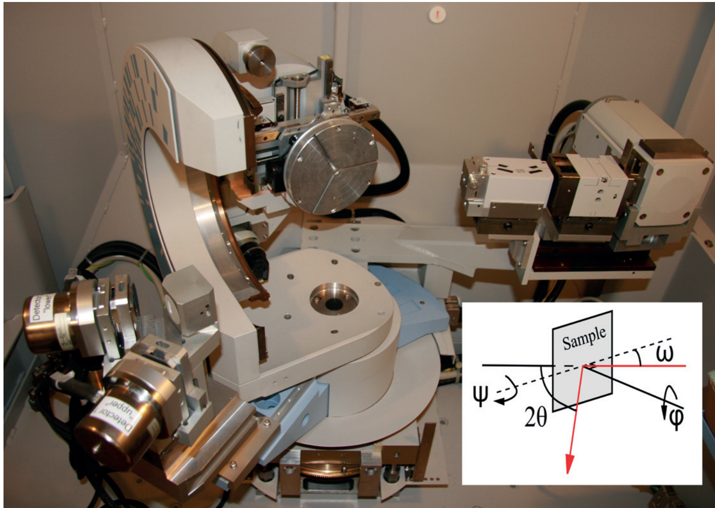

Figure 4.1. XRD apparatus and the schematical drawing of the different angles that can be altered during the measurement. The red line is the X-ray beam coming from the X-ray source to the detector.

tance fixed by moving the sample vertically with the piezoelectric sample holder with the help of the feedback signal. The information about the sample morphology is then obtained from the feedback signal.

4.2 X-ray diffraction

X-ray diffraction (XRD) is an experimental method used to examine the crystal structure of materials. In the XRD measurement, a monochromatic beam of X-rays hits the sample and diffracts, reflects or scatters depending on the measurement geometry. The intensity of the diffracted rays is measured with the detector from different angles. Structural information of the sample can be extracted from the measured curve. Fig. 4.1 shows a photograph of the used Philips X'pert Pro MRD diffractometer which is comprised of a X-ray generator producing $Cu_{K_{\alpha,1}}$ radiation, X-ray optics, a goniometer, a detector and a computer. In addition, also the different measurement angles are illustrated schematically in the inset of Fig. 4.1: 2θ being the angle between the diffracting and transmitting beams, ω the angle between the sample surface and the incident beam, ϕ the angle rotating the sample azimuth, and ψ the angle tilting the normal of the sample.

4.2.1 Bragg's law and its utilization in XRD measurements

A monochromatic beam of X-rays scatters from the atoms of a crystal and forms a constructive interference in certain angles. Bragg's law states that the highest intensity of the diffracted radiation is found at angles of θ satisfying

$$2d \sin\theta = \lambda, \tag{4.1}$$

where $d = a/\sqrt{h^2+k^2+l^2}$ is the spacing between the diffracting (hkl) crystal planes of the zinc blende crystal lattice with lattice constant a and λ the wavelength of the X-ray radiation. Information from the lattice constant of the crystal can be obtained by 2θ-ω measurements. In this measurement, both the 2θ and ω angles of the apparatus are changed simultaneously to achieve the diffracted intensity as a function of the diffraction angle θ. In this thesis, 2θ-ω measurements were performed in high-resolution and powder setups. The benefits of these setups differ, and thus, the selection between the two depends on the sample.

High-resolution XRD measurements were performed on epitaxial films. The angular resolution of this setup is extremely high which enables defining the thickness and the lattice constant of the layers, and as a result, the strain state and the composition of the crystal accurately. For this thesis, HRXRD measurements were performed using a triple-axis geometry at the diffracted beam side with an analyzer crystal acceptance angle of 12 arcsecs. At the incident beam side, the X-ray beam was guided through an X-ray mirror and monochromatized with four Ge (220) crystals.

The powder XRD setup is typically used for examining the materials with a non-perfect crystal structure and orientation. In this thesis, powder XRD setup was chosen for the structural studies of the nanowire samples. Typically, powder XRD measurements are performed to polycrystalline or powder samples, hence the name. The crystallites inside these type of samples are tilted with respect to each other. The powder XRD setup is well suited for XRD studies of these samples due to the poor X-ray optics of the setup and high X-ray radiation intensity. The poor optics guarantees that there always exists some crystallites that are aligned in such a way that the Bragg's condition can be fulfilled and the information concerning the crystal structure gathered. The optics of the powder XRD setup consists of only two slits, one in front of the detector and another in front of the X-ray source, which are opened during the measurement to

radiate the same area of the sample in every measurement angle.

4.2.2 Transverse scan measurements

In X-ray diffraction rocking curve measurements, the 2θ angle is fixed in the Bragg angle and the diffracted intensity from the sample is measured by rocking the ω angle. As a result, rocking curve measurements contain the information from the crystal disorder which affects the width and the shape of the peak of the rocking curve. The disorder may originate from many sources such as crystal defects, substrate curvature, mosaicity, and also phonon vibrations [12]. In order to extract this information, transverse scan measurements were performed. The transverse scan measurement refers to the measurement of a high-resolution rocking curve and is performed with the similar setup than the setup used in the high-resolution XRD measurements. Transverse scan line profiles can possess two-component lineshapes in which the narrow component is the Bragg peak of the sample (originating from long-range structural correlations), and the broad component arises from diffuse scattering and contains information about the disorder in the crystals. In rocking curve measurements (omega-scan performed with an open detector), the broad and narrow components typically overlap. In this thesis, the transverse scan analysis (omega-scan performed with a back monochromator) was performed to examine the broadening of the rocking curve and to extract information relating to the antiphase disorder in GaP layers grown on silicon with the method presented by Létoublon *et. al* [13]. This method is described in more detail in chapter 5.

4.2.3 Synchrotron XRD topography

X-ray diffraction topography refers to the experimental method in which X-ray images are taken from crystalline samples utilizing diffraction. In the X-ray topographs, atoms act as scattering centers, and thus, the strain field surrounding the crystal defects forms a contrast difference in the image. In the case of a small enough ($< 10^4$cm^{-2}) defect density, different type of crystalline defects such as misfit and threading dislocations, stacking faults, twin faults, voids, precipitates, and magnetic domains can be resolved from the topographs. For a more detailed review of the technique see Ref. [14].

X-ray topographs were recorded on high-resolution X-ray films (Slavich

VRP-M) using synchrotron radiation at the Hasylab beamline F1 in Hamburg. The X-ray beam emitted by a bending magnet source of the positron storage ring has a wide spectrum of wavelengths guaranteeing that there exist wavelengths for many different Bragg reflections. Therefore, the X-ray beam is diffracted by a number of lattice planes and there is no need to align the sample into a specific orientation. Back reflection and transmission X-ray topographs were recorded aligning the sample so that the horizontal direction corresponded to the <110> direction and the [001] crystal direction was held in a 12° angle with respect to the incident beam. The distance between the film and the sample was 60 mm.

4.3 Rutherford backscattering spectroscopy

Rutherford backscattering spectroscopy (RBS) combined with nuclear reaction analysis (NRA) measurements were performed to study the composition and the point defects of the GaPN layers. RBS reveals comparable information to that what XRD reveals, but combined with NRA it is possible to measure the distribution and configuration of nitrogen atoms in the GaPN layers. Thus, the technique guarantees interesting information relating to the point defects of the material. All RBS and NRA measurements presented in this thesis were performed at Lawrence Berkley National Laboratory by Dr. Kin Man Yu.

The $^{14}N(\alpha,p)^{17}O$ reaction with a 3.72 MeV $^{4}He^{2+}$ beam was used for detection of nitrogen. A 150 mm^2 passivated implanted planar silicon (PIPS) detector with a $3\times$ 12 mm slit was used to detect the emitted protons at a 135° angle with respect to the incident beam. A 25 μm thick mylar foil was placed in front of the detector to absorb the backscattered α particles. The N content in the film was obtained by the total proton yields analyzed by the SIMNRA software package [15] with a thin InN sample as a reference for absolute quantification. RBS spectra were also obtained simultaneously at 168° with another PIPS detector. Both RBS and NRA measurements were carried out in random as well as in <100> and <110> axial channeling directions. The fraction of substitutional nitrogen atoms in the films, f_{sub}, as well as the interstitial fraction, f_I, and the random fraction, f_{rand}, was obtained by comparing the random and channeling yields of the RBS and the NRA measurements along the different channeling directions.

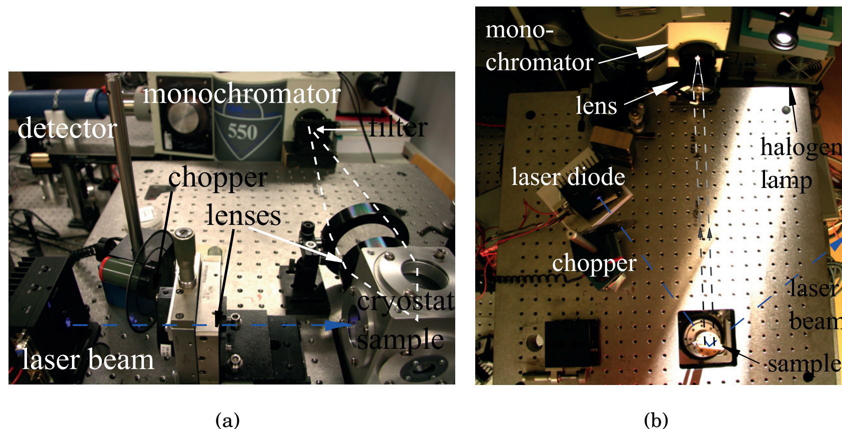

(a) (b)

Figure 4.2. (a) Photoluminescence and (b) photoreflectance setups were used to characterize the energy band structure of the semiconductor materials. The cryostat which is used to change the measurement temperature is removed from the image of the PR setup for clarity.

4.4 Optical spectroscopy

Optical spectroscopy methods are used to examine the energy band structure of the material. Photoluminescence (PL) measurements gather the information on the spectra of the emitted photons. Photoreflectance (PR) spectroscopy, on the other hand, is a modulation spectroscopy measurement and reveals directly all direct transitions between any states of the material that possess a sufficient density of state.

4.4.1 Photoluminescence

Photoluminescence is an optical spectroscopy method used for the examination of energy states in semiconductor materials. In photoluminescence measurements, laser beam is absorbed in the sample exciting charge carriers from the lower energy states to the higher energy states. After this the excited charge carriers thermalize to certain energy minima and, then, recombine either radiatively or non-radiatively. The energy of the generated photons correspond to the differences between the participating states in the sample (*e.g.*, between the conduction band minimum and valence band maximum).

The PL measurement setup used in this thesis is presented in Fig. 4.2. The setup is comprised of a laser (typically an InGaN laser diode with the wavelength of 405 nm), a photodetector (typically Hamamatsu R928 photomultiplier tube), a lock-in amplifier, a monochromator, and a cryostat.

During the measurement, the samples are placed inside the cryostat. The temperature of the cryostat can be changed between 8 K and 300 K. The excitation beam from the InGaN laser diode is guided through the chopper to the sample surface. Photons emitted to a definite cone are collected to the monochromator by lenses. The reflected laser beam is filtered away before it enters the monochromator. The monochromator allows only a certain wavelength of the emission spectrum to be transmitted through at a time. The detector is located at the output of the monocromator and measures the intensity of the transmitted photons. The use of a lock-in amplifier improves the signal-to-noise ratio by phase-locking the detector output and the reference signal from the chopper. The measurement data is collected and stored in the computer.

4.4.2 Photoreflectance

Photoreflectance belongs to the family of modulation spectroscopy methods and is a powerful tool for the characterization of the band structure of semiconductor materials. PR measures the change in reflected light when the sample is photomodulated. Photomodulation changes the carrier density of the sample surface, and thus, modulates the surface electric field. It has been shown that the PR spectrum is proportional to the third derivative of the dielectric function of the material [16]. The changes in the dielectric function are the strongest near the critical points of the band structure, *i.e.*, at energies corresponding to direct band-to-band transitions. Therefore, oscillations are created at these locations of the PR spectrum, and in theory, all direct transition energies of the material can be resolved. Note that due to this reason PR spectroscopy reveals more information related to the band structure of the material than the PL spectroscopy which observes only the energy states in which charge carriers thermalize and after that recombine radiatively. The accuracy of the PR measurement is based on the derivative nature of the spectrum and the well-known lineshapes of different transitions. Thus, the position and the type of the transition requires comparison between the experimentally measured and the simulated PR curve.

PR measurements performed for this thesis were carried out in a bright configuration placing a monochromator between the silicon detector and the sample. The sample can be placed inside a cryostat for altering the measurement temperature. Broad spectrum light was produced by a halogen lamp and the surface electric field was modulated by chopping the 405

nm InGaN laser diode beam with the frequency of 375 Hz. The signal was measured by standard lock-in techniques. The setup of the PR measurement is presented in detail in Fig. 4.2. The information from the photoreflectance curves was obtained by fitting a PR line shape to the measured photoreflectance spectra with the Monte Carlo method. This method was used because the fitted formula contained at maximum 18 free parameters. In the Monte Carlo method, the fitting procedure performed by the Metropolis algorithm was repeated 100 times. The benefit of the method is that the obtained values are the averages of the every separate result of the fitting, and thus, the magnitude of the possible fitting error reduces. In addition, the reliability of the method can be estimated from the standard deviation of the separate 100 fitting parameters, and it was observed to be good.

4.5 Capacitance voltage characterization and the Terman method

The capacitance voltage (CV) measurement is a powerful tool revealing information on the electrical properties of semiconductor structures. For a more detailed review see Ref. [17]. The CV measurement requires a semiconductor structure with a depletion region, *i.e.*, a region empty of conducting charge carriers. Thus, CV measurements are typically performed to Schottky diodes, pn-junctions or MIS capacitors. The information that the CV measurement provides relates to the properties affecting the depletion layer capacitance. Therefore, it is possible to examine, *e.g.*, the doping concentration of the material or even the trap states affecting the properties of the MIS capacitor. In this thesis, high frequency CV characterization was carried out to fabricated GaAs MIS structures to study the properties of the semiconductor/insulator interface.

High-frequency CV curves were measured using a HP-4192A impedance analyzer. The CV measurement was performed biasing the metal plate of the MIS capacitor and sweeping it from -4 V to 4 V with the sweep rate of 100 mV/s. The real and imaginary parts of the circuit impedance were recorded as a function of bias voltage. The AC frequency used in the measurement was 100 kHz and the amplitude was 25 mV. In some of the measurements, a microscope lamp was used as a light source to enhance the generation rate of the charge carriers. In addition, a resistive heater was used for the same purpose. The measured admittance values were corrected with the formulas obtained from the equivalent circuit model

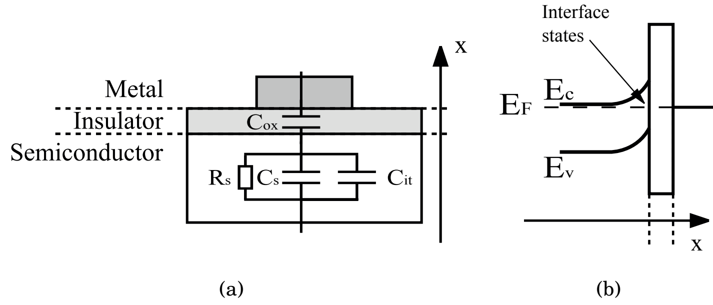

Figure 4.3. (a) Equivalent circuit of a MIS capacitor at low-frequency. When the measurement is performed at high-frequency the interface trap capacitance C_{it} is not directly contributing to the overall capacitance value. (b) The energy band structure of the MIS capacitor illustrated schematically.

which is shown in Fig. 4.3 [17, 18].

To extract information from the band bending at the GaAs/insulator interface and the presence of interface traps a high frequency CV curve needs to be simulated. Many programs exist for simulating the CV curves of silicon based MOS capacitors. However, due to the different band structures of silicon and III-V compounds (causing that some approximations are invalid for the latter materials) the simulation was performed numerically with the method presented by Engel-Herbert *et al.* [18]. Thus, a *MATLAB* program was written which solved the semiconductor capacitance, C_s, as a function of band bending and gate bias. The calculation of the total charge per unit area in the semiconductor as a function of band bending, the derivative of which the semiconductor capacitance is, was performed by integrating the Poisson equation to obtain the surface electric field and then applying the Gauss's law. The required charge carrier densities were calculated utilizing the Fermi-dirac distribution and density of states functions briefly mentioned in Chapter 2.

5. Integration of III-V compounds on silicon: monolithic growth of GaP layers and vapor-liquid-solid growth of GaAs nanowires

As mentioned, integration of III-V compounds on silicon substrates may enable new possibilities for semiconductor industry to realize interesting device concepts. Therefore, many methods have been developed to integrate III-V compound semiconductor layers on silicon substrates. In this chapter, a few typically used approaches are reviewed and the integration methods studied in this thesis are presented.

5.1 Common integration approaches

The most commonly used approach in the industry is the wafer bonding in which III-V compound semiconductor devices are bonded on silicon substrates. The benefit of this approach is that the crystal defects arising from the III-V compound/silicon interface can be avoided, and therefore, high-quality components can be realized on silicon platforms. Despite this fact the bonding also adds difficulties to the fabrication process. Some bonding techniques require high temperatures, and thus, due to differences between the thermal expansion coefficients of the bonded materials, thermal strain may prevent successful bonding. In addition, the lateral control of the position of the devices is not that precise, and therefore, certain size limitations exist. This can be a major issue for some potential device concepts as the silicon technology attempts to continously proceed to even smaller dimensions. Another disadvantage is that in addition to silicon substrates III-V compound substrates have to be used which significantly increases the fabrication costs. Despite the challenges optoelectronic integrated circuits have been realized on silicon substrates using this approach. For instance, InP and GaAs based light emitters have been integrated on silicon CMOS circuits [19, 20]. In addition, this approach is considered as a one possible way to integrate high-mobility

III-V compound materials on silicon based IC chips.

Monolithic integration of III-V compound semiconductors and silicon would be the most elegant concept. In monolithic integration III-V layers are directly fabricated epitaxially on silicon substrate (see Fig. 5.1(b)). The benefit of this concept is that the grown layer should be identical throughout the whole wafer, and therefore, no specific alignment is required for later processing steps. Despite all the theoretical advantages, however, very few reports exist in the literature in which the monolithic integration of high-quality III-V compound semiconductor layers, mainly from gallium phosphide, have been demonstrated [7–9, 21]. To list a few examples in addition to GaP layers at least GaAs [22, 23], InAs [24], InP [25], GaSb [26] and GaN [21] layers have been grown on silicon substrates. The difficulties of the monolithic growth arise from the III-V compound/silicon interface[1]. For instance, typical crystal defects originating from the interface comprise antiphase domains, stacking faults, threading and misfit dislocations and twin faults. In order to prevent the formation of these defects, much care is required to obtain an optimal surface reconstruction for the silicon surface prior the growth. For instance, Volz *et al.* have reported that to obtain a defect-free GaP buffer layer on silicon three steps must be performed. Firstly, a silicon buffer layer is required to be deposited; secondly, the buffer layer to be annealed at right conditions to obtain bi-atomically stepped surface; and then thirdly, the growth to be started by migration enhanced epitaxy growth mode in which precursors are supplied in turns inside the MOVPE reactor [8]. This exemplifies the complexity of the monolithic growth. However, as mentioned previously high quality GaP layers have been used for instance as a buffer layer on which electrically pumped lasers and LEDs have been fabricated from GaAsPN QWs and InGaAs QDs, respectively [10, 27]. In addition, GaP buffer layers have been used to grow high electron mobility InAs layers for high mobility transistor applications [28] and GaAsP layers for tandem solar cells [4]. The monolithic growth of GaP layers on silicon was studied in Publication I and II.

Epitaxial lateral overgrowth (ELOG) is another integration concept and briefly mentioned here because it is a quite widely studied technique to reduce the defect density in the fabricated III-V compound semiconductor layers. Typically, ELOG has been used in the fabrication of III-V com-

[1] ...and are well presented in an old review paper dealing with the growth of GaAs on silicon, see Ref. 22

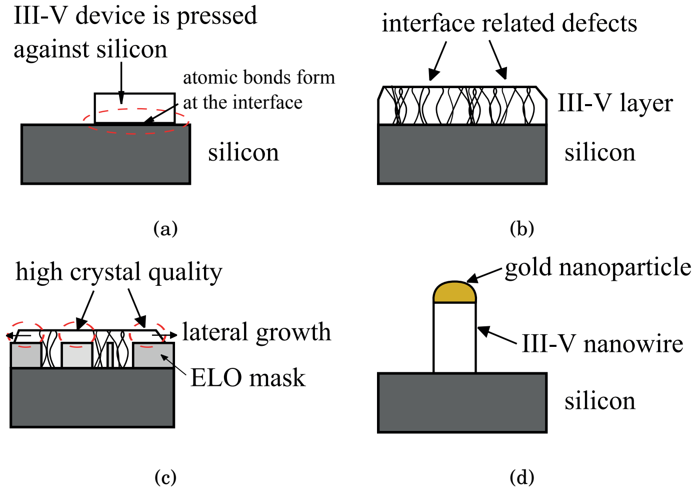

Figure 5.1. Schematics of the approaches used to integrate III-V compound semiconductors on silicon: (a) wafer bonding, (b) monolithic growth, (c) epitaxial lateral overgrowth and (d) VLS nanowires.

pound materials with large lattice mismatch on silicon (*e.g.*, InP [29–31], GaAs [32] and GaN [33]). Fig. 5.1(c) shows schematically the ELOG process. In ELOG, an amorphous masking layer (*e.g.*, aluminum oxide) is deposited on the silicon substrate, patterned and removed from some positions. Then, the epitaxial growth occurs at the positions from which the masking layer is removed. The layer grows first through the mask and then starts to grow laterally. The quality of the grown layer is weak over the positions where no mask exists. This is due to the III-V compound/silicon interface which creates many defects to the ELOG layer. However, these interface related defects are not copied to the part of the layer forming due to the lateral overgrowth.

The final approach discussed in this thesis is the nanowire growth via vapor-liquid-solid (VLS) growth mechanism (Fig. 5.1(d)) [34]. The VLS growth mode enables the fabrication of III-V compound nanowires on silicon and also even on amorphous low-cost substrates such as glass (see Publication III). The VLS growth occurs in such a way that at first metal nanoparticles (dimension of the particles around 50 nm), which act as catalysts for the growth, are deposited on the silicon substrate and then the substrate is placed inside the MOVPE reactor. The substrate is heated causing the melting of the metal nanoparticles. Then, the group III source materials, which are supplied to the reactor in addition to the group V source materials, are absorbed inside the metal droplets. The supersaturation of the group III source materials inside the liquid metal nanopar-

ticles causes the III-V compound semiconductor nanowire growth to start under the metal droplets. The benefit of the VLS concept is that all the issues arising from the III-V compound/silicon interface do not play that significant role because of the small diameter of the nanowire. The strain due to the lattice mismatch accommodates laterally and also no APDs have been observed in nanowires. However, stacking faults and twin faults may form in the grown nanowires, but their density can be suppressed by altering the growth parameters [35]. The disadvantage of the nanowire growth is that nanowires will form at random positions. Thus, complex processing techniques are required to realize semiconductor devices from nanowires, and for instance, even the fabrication of the metal contacts is challenging. In addition, due to the favoured [111] growth direction of the nanowires it is preferable to use (111)-oriented silicon as a growth substrate. This adds limitations because commonly the silicon industry uses (001) oriented wafers. However, despite all the limitations semiconductor devices such as field-effect transistors have been fabricated from VLS grown nanowires [36]. In addition, quite recently the solar cell operation with an efficiency of 14% was demonstrated from InP nanowires, thus exemplyfying the potential of the VLS approach [37].

5.2 Monolithic integration of GaP on silicon

In Publication I and II, monolithic growth of GaP layers on silicon substrates was studied to fabricate III-V compound semiconductor buffer layer on silicon. The benefit of using GaP is its nearly similar lattice constant compared to silicon (lattice mismatch of 0.37% at room temperature) which should enable the growth of an approximately 100 nm thick layer without formation of misfit dislocations [38]. This thickness has been demonstrated to be enough to suppress the propagation of the interface related defects to the above layers [8].

5.2.1 AFM studies of GaP layers on silicon

Despite the small lattice mismatch the growth of GaP on silicon is a difficult task due to many other differences between the materials. Successful growth requires solving the issues created by the polarity difference between the materials, the favoured three-dimensional growth mode and the charge neutrality along the interface [7, 9, 39, 40]. Fig. 5.2 shows

AFM images of GaP layers grown on silicon. All substrates used in these studies were (001) silicon wafers without any offcut unless otherwise mentioned. Prior to the growth, the silicon substrates were etched in HF:H_2O (1:10) solution to remove the native oxide of the silicon wafer. If this was not performed no layer-by-layer growth mode occurred and the grown layer was comprised of large clusters (Fig. 5.2(a)).

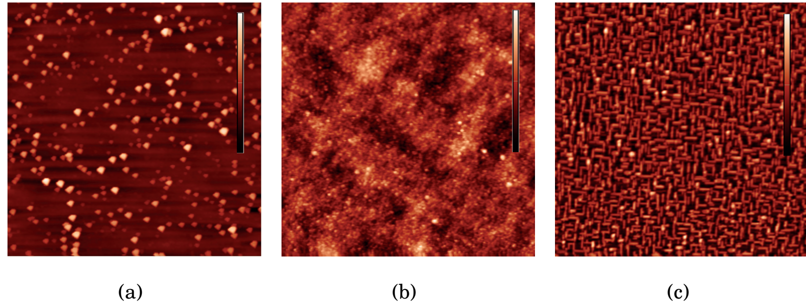

(a) (b) (c)

Figure 5.2. Atomic force microscope images of nominally 5 nm thick GaP layers grown at 475°C on silicon substrate (a) without and (b) with HF dip, and (c) a 40 nm thick GaP layer grown at 700°C. The size of the image is 2×2 μm^2, 2×2 μm^2, and 10×10 μm^2, and the colorbar corresponds to 55 nm, 4 nm, and 100 nm, respectively.

The growth temperature affects the layer morphology. Fig. 5.2(b) shows an AFM image of a GaP layer grown at 475°C from which one can see that a relatively smooth layer can be obtained. However, the growth rate at 475°C is extremely slow due to incomplete pyrolysis of the source materials. Therefore, the effect of increased growth temperature was also examined. Fig. 5.2(c) shows an AFM image of a GaP layer grown at 700°C and it can be seen that the layer consists of a net of horizontal GaP wires pointing at <110> crystal directions. In Publication II, it was proposed that this type of growth mode occurs due to anisotropic diffusion of the adatoms and the smaller surface energy of silicon than GaP. In addition, it should be noted that the wire growth mode is most probably affected by other factors as well such as strain. However, whatever is the reason, high diffusion created by the high growth temperature enables Ga and P adatoms to form these horizontal wires. As a result of these observations, the growth process was designed in such a way that after a 5 nm thick buffer layer had been fabricated and the silicon surface covered with GaP the growth temperature was increased to 700°C.

Fig. 5.3 shows AFM images of 70 nm thick GaP layers grown at 700°C and at 680°C on 5 nm thick GaP layers deposited on exactly oriented and on 4 degree misoriented (towards [110] direction) silicon (001) substrates,

respectively. All the layer thicknesses were measured by X-ray reflection. AFM images show that a layer-by-layer growth mode is obtained and that the low temperature buffer layer prevents the formation of a net-of-wires type structure. In addition, the substrate crystal orientation affects the morphology of the GaP layers. The GaP layer on the exactly-oriented silicon substrate is comprised of terraces. On the other hand, the GaP layer on the misoriented silicon substrate is composed of hillocks whose morphology can be affected by the growth temperature.

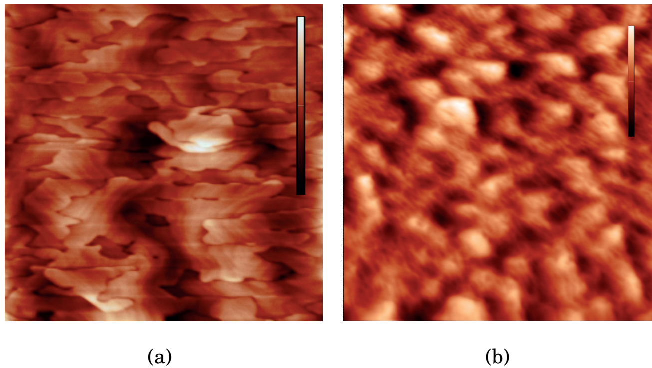

(a) (b)

Figure 5.3. Atomic force microscope images of 70 nm thick GaP layers grown on a low-temperature GaP nucleation layer deposited on (a) exactly oriented and (b) 4 degrees misoriented silicon (001) substrates. Horizontal directions of the both AFM image correspond to one of the [110] directions. The size of the image is 2×2 μm^2 and 5×5 μm^2 and the colorbar corresponds to 7 nm and 15 nm, respectively.

AFM studies showed that the growth of GaP needs to be started at low temperatures to obtain layer-by-layer growth. In addition, a careful substrate preparation is required prior to the epitaxial growth to obtain smooth layers. However, it should be noted that no atomic steps were observed on the surface of the grown GaP layers most likely due to GaP/silicon interface related defects. In order to fabricate smoother layers, the fabrication technique probably needs to be developed more to the direction presented by Volz *et al.* [8]. This, however, would require a different MOVPE apparatus supplied with precursors decomposing more effectively at lower temperatures and also the possibility to anneal and grow silicon at different pressures and at higher temperatures than the current maximum temperature of the used MOVPE apparatus of 855°C.

5.2.2 Structural study of thin GaP layers on silicon by transverse scan analysis

The studies relating to the crystal quality of III-V compound semiconductor layers on silicon substrates are typically performed by transmission electron microscopy (*e.g.*, for characterization of antiphase disorder see Refs. [39, 41]). In this thesis, these studies were performed by high-resolution XRD measurements recording transverse scan line profiles (see Publication I). The transverse scan refers to the measurement of a high resolution rocking curve and was quite recently proposed by Létoublon *et al.* to be used for the characterization of antiphase disorder in GaP layers on silicon substrates [13]. The formation of antiphase domains occurs mainly because the atomic steps of the silicon substrate affect the polarity of the crystal differently depending on the location with respect to the atomic step edge (see Fig. 2.2). In order to obtain antiphase domain free layers the silicon surface should be composed of atomic steps of bi-atomic height prior to growth. It is well known that the formation of bi-atomic steps is thermodynamically favored on misoriented silicon substrates [22]. In addition, it has been demonstrated that the formation of bi-atomic steps can be affected artificially by annealing [40]. However, despite the fact that the probability for bi-atomic step formation increases in these cases it is still likely that monoatomic steps exist on all silicon substrates.

In Publication I, the measured transverse scan curves were plotted in reciprocal space units obtained by the following formulas:

$$S = \frac{2}{\lambda}\sin(\frac{2\theta}{2}), \tag{5.1}$$

$$S_x = S\sin(\omega - \omega_B), \tag{5.2}$$

where S is the diffraction vector length and S_x the diffraction vector component along the crystal plane. In addition, ω_B is the ω angle corresponding to the diffraction maximum of the reflection.

Fig. 5.4 shows the transverse scan line profiles for $(00l)$ reflections $(l = 2, 4, 6)$ measured from the GaP layers grown on exactly oriented and 4 degree misoriented silicon subsrates. The AFM images of these samples were presented in Fig. 5.3. It can be observed that the transverse scan line profiles possess a two-component line shape and are clearly broadened differently. In addition, satellite peaks are observed in the (002) transverse scans of the GaP layers on the exactly oriented silicon substrate and can also be recognized from the (006) reflection. In Publication

I, two parameters were extracted from the transverse scan line profiles in order to obtain information from the origin of the crystal disorder affecting the line shape broadening: (i) the integral breadth (IB) of the broad component, and (ii) the quality factor (QF) of the line profile, defined as the ratio between the areas of the thin and broad components. These parameters were extracted by fitting two pseudo-Voigt functions to the measured curves.

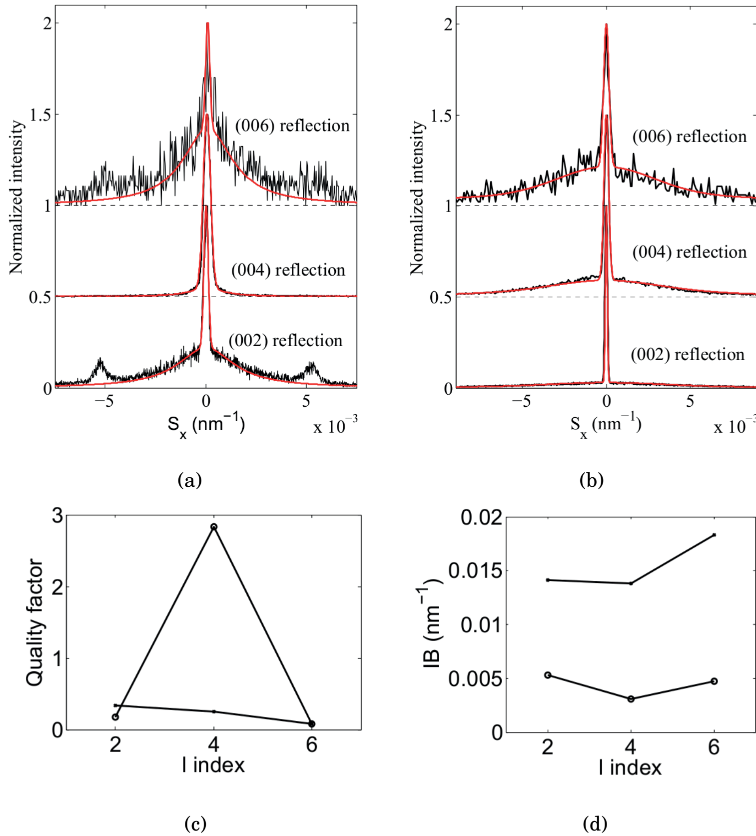

Figure 5.4. Measured transverse scan line profiles from GaP layers on (a) exactly-oriented and (b) 4 degrees misoriented silicon (001) substrates. In the measurement, the diffraction vector component S_X is along a direction perpendicular to atomic steps of silicon substrate. The fitted curves are plotted with red lines. The QF (c) and the IB (d) information extracted from the fitting (drawn with (o) for exactly oriented and with (·) for misoriented substrates) is plotted as a function of reflection index.

Different types of defects create different types of disorder which may broaden the transverse scan line profiles differently. More information can be found in Refs. [42–46] or a more detailed review in Ref. [12]. In this thesis, the transverse scan line profiles were used to extract information about the antiphase disorder, the presence of which affects the diffuse

scattering of the APD sensitive (002) and (006) reflections [12, 13]. It has been shown that when antiphase disorder exists in GaP layers the QF of the APD sensitive reflection is significantly lower than the QF of the APD insensitive (004) reflection [13]. Therefore, the presence of APDs was evaluated by comparing the QF of the APD sensitive reflection to the QF of the APD insensitive reflection. In addition, it has been shown that the integral breadth of the APD sensitive reflections defines the lateral correlation length of crystalline defects which in this case corresponds to the size of the APDs [13].

Fig. 5.4 clearly shows that the QF of the APD sensitive (002) and (006) reflections of the GaP layer on the exactly-oriented silicon substrate is smaller than that of the QF of the APD insensitive (004) reflection. Therefore, it was concluded in Publication I that antiphase disorder exists in the GaP layer on the exactly oriented substrate and that the IB gives a lateral correlation length of 150 nm. The size of the correlation length is comparable to the size of terraces observed in the AFM images (see Fig. 5.3), and thus, the observed terraces most likely correspond to APDs. The transverse scan profiles of the GaP layers on misoriented silicon substrates did not show similar APD induced broadening, and therefore, it was proposed in Publication I that the broadening behavior resembles more the broadening behavior at the weak disorder limit. The weak disorder is most likely induced by threading dislocations and stacking fault type defects. However, it should be noted that small antiphase domains which are beyond the resolution limit of this measurement technique may exist in these GaP layers as well.

Satellite peaks are sometimes observed in transverse scan measurements and can originate from very strong short range correlations (*e.g.*, from misfit dislocation network) [46]. In Publication I, the origin of the satellite peaks observed in the (002) and (006) reflections was examined performing transverse scans also at an azimuth angle, $\phi = 90^\circ$, perpendicular to the first measurement. In this case, satellite peaks were not observed. As a result, if these satellite peaks would originate from dislocations it would mean that they should be observed at every azimuth angle or that the strong correlation between dislocations would only be along one direction. To study this issue further, back-reflection X-ray diffraction topographs were measured with synchrotron radiation. No dislocations were observed implying that either the density of these dislocations was beyond the resolution limit or that the satellite peaks originated from

other type of defects. It was suggested that the origin of the satellite peaks is most likely periodic distortion arising from the terraces on the surface of the substrate, and thus, may also be related to antiphase disorder.

5.3 GaAs nanowires on silicon and low-cost glass substrates

In Publication III and IV, the growth of GaAs nanowires was studied on non III-V compound semiconductor substrates. The used substrates were silicon, glass and aluminum doped zinc oxide (AZO) layers on silicon. The possibility to use other than III-V compound semiconductor substrates provides the opportunity to fabricate semiconductor devices on practically any substrate. For instance, AZO can be deposited by atomic layer deposition (ALD) even on low-cost aluminum foil on which the nanowires could then be realized by the VLS growth mode.

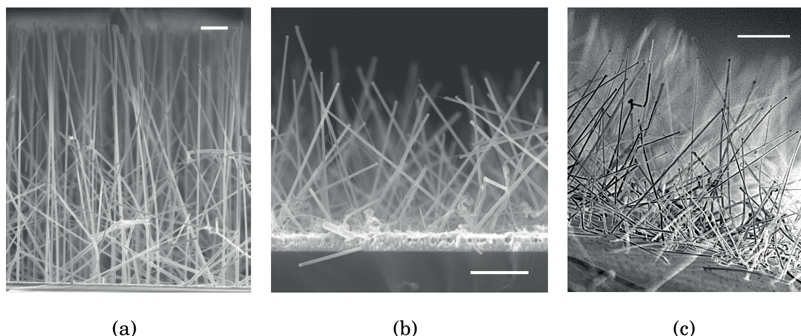

(a) (b) (c)

Figure 5.5. SEM images of GaAs nanowires grown on (a) silicon and (c) glass substrates, and (b) on aluminum doped zinc oxide layers. The thick white line corresponds to distance of (a) 2 μm, (b) 1 μm and (c) 2 μm.

Fig. 5.5 presents the SEM images of GaAs nanowires on silicon, glass and AZO layers on silicon. SEM images show that the nanowires were grown successfully on all of these substrates. However, the fabricated nanowires are not aligned perfectly vertically on silicon and point towards random directions on non-crystalline substrates. Typically, nanowires tend to grow along <111> crystal directions and vertically aligned III-V compound semiconductor nanowires have been fabricated via 'homoepitaxy' on (111) oriented compound semiconductor substrates (*e.g.*, InP nanowires on (111) InP substrates) [47]. To explain the tilting of the grown GaAs nanowires it should be noted that at least the strain due to the lattice mismatch between GaAs and silicon and also the amorphous/polycrystalline nature of glass and AZO substrates may cause the non-vertical

growth. This is important to mention because from a device fabrication point-of-view perfectly vertically aligned nanowires are preferred making the latter processing steps easier.

The crystal structure of the nanowires was studied by powder x-ray diffraction measurements and transmission electron microscopy. Usually, the crystallinity of nanowires is studied only by transmission electron microscopy because it may be difficult to obtain a distinct XRD signal due to the non-uniform alignment and small volume of the nanowires. However, the powder XRD setup is well suited for the measurement due to reasons explained in Chapter 4. Fig. 5.6 shows the powder XRD profiles measured from GaAs nanowire samples fabricated on different substrates. The XRD peaks located at 27.3°, 45.4° and 53.7° originate from GaAs (111), (220) and (311) crystal planes, respectively, indicating that the nanowires are crystalline zinc-blende GaAs. The other XRD peaks in Fig. 5.6 originate from the crystal planes of the silicon substrate and aluminum doped zinc oxide layers. Note that the (220) and (311) diffraction peaks are not visible in the powder XRD spectrum of GaAs nanowires grown on silicon. This can be explained by the more uniform alignment of the nanowires.

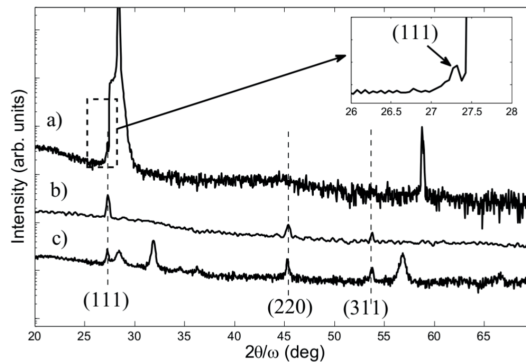

Figure 5.6. Powder XRD patterns of GaAs nanowires grown on (a) silicon, (b) glass and (c) AZO layers on silicon. The locations of angles corresponding to different GaAs crystal planes are illustrated with dashed lines. The powder XRD profiles of GaAs nanowires on AZO and on silicon show diffraction peaks from AZO and silicon as well.

The crystallinity of nanowires was also examined by transmission electron microscopy and the results of the both measurement techniques agreed. It should be noted that transmission electron microscopy provides more detailed information about the crystal structures and defects of the specimen but can only be used to probe a single wire at a time. For instance, stacking faults and micro twins were observed in Publication IV from

GaAs nanowires on AZO. However, the benefit of using the both techniques is that, as TEM provides extremely detailed information from random wires, a more statistical analysis throughout the whole sample can be verified by the powder XRD.

In addition, note that sometimes GaAs nanowires or a portion of them crystallize in the wurtzite crystal structure. In the powder XRD studies, no peaks originating from the wurtzite phase was observed indicating that the grown nanowires are either pure zinc-blende or that the volume of the wurtzite phase is beyond the resolution of the powder XRD measurement. The optical properties of wurtzite GaAs are not that good, and thus, the observation of only zinc-blende nanowires is promising. In addition, it should be noted that the optical properties were better when the nanowires were grown on AZO and glass than on silicon. This observation was different than expected and may be related to some energy states of impurity atoms (*e.g.*, zinc) participating in the luminescence processes or impurity atoms creating a mean for surface passivation. However, more systematic work is required to address the cause for this observation.

6. Characterization of Ga(As)PN materials

High-quality layers from III-V compound semiconductor materials can be grown on GaP buffer layers on silicon if the buffer layer prevents the propagation of most of the GaP/silicon interface related defects. However, in order to fabricate semiconductor devices from these layers the total thickness of the grown materials needs to be a few micrometers in many applications. Therefore, the issues arising from the strain due to the lattice mismatch have to be maintained in controlled fashion.

Fig. 6.1 shows the band gap energy of many different III-V compound semiconductor materials as a function of their lattice constant. Since most of the III-V compounds possess larger lattice constants than silicon the lattice strain cannot be compensated by alloying Ga(As)P with the many typical group III and group V atoms. However, few exceptions exist and it has been shown that the strain can be compensated by alloying GaAsP with nitrogen and GaP with boron [48]. For instance, this approach was used in the fabrication of the first monolithically integrated electrically pumped high quality laser diode on a silicon substrate [10]. In addition, GaAsPN lattice-matched to silicon has been proposed to be used in the fabrication of silicon tandem solar cells [49].

This chapter is organized in such a way that first the structural studies performed to Ga(As)PN layers are presented and then the observations gathered from the energy band structure are described. The discussion follows the work presented in Publication V, VI and VII. The structural properties of GaPN based materials were studied by X-ray diffraction topography, positron annihilation spectroscopy and Rutherford backscattering spectroscopy combined with nuclear reaction analysis. The energy band structure was examined by photoreflectance and photoluminescence measurements. In all of these studies, the GaPN layers were grown on GaP substrates by MOVPE to extract the issues created by nitrogen al-

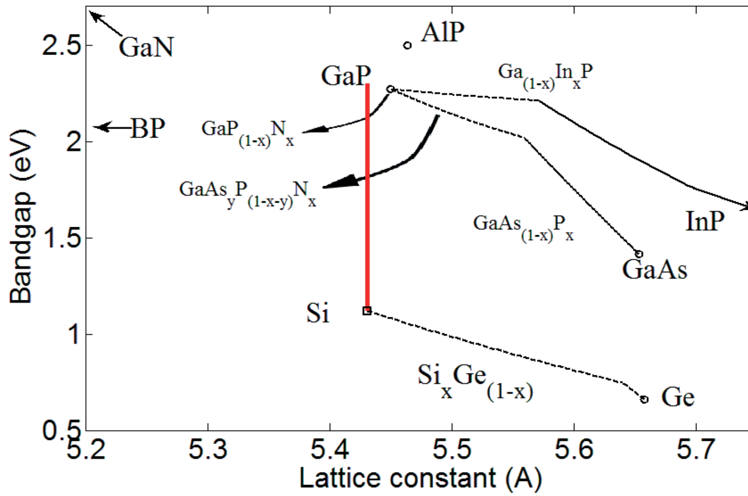

Figure 6.1. Band gap energy of various III-V compound semiconductor materials and their alloys as a function of the lattice constant. Band gap energy and lattice constant of silicon and germanium are also shown. Dashed and solid lines illustrate indirect and direct band gap, respectively. Red line corresponds to the lattice constant of silicon.

loying from the GaP/silicon interface related defects. In Publication VII, the strain compensation of GaPN based layers grown on silicon substrates was examined by Raman and XRD measurements.

6.1 Structural properties of GaPN alloys

6.1.1 Strain relaxation in GaPN layers on GaP substrates

In Publication V, a series of $GaP_{0.98}N_{0.02}$ layers with different thicknesses was grown on GaP substrates to examine the strain relaxation in GaPN layers. The composition and the layer thickness of different samples were measured by high-resolution XRD. Back reflection X-ray topographs were recorded to study the formation of misfit dislocations at the interface between the $GaP_{0.98}N_{0.02}$ layer and the GaP substrate. Fig. 6.2 shows the 004 back reflection topographs of three $GaP_{0.98}N_{0.02}$ samples with different thicknesses. Two types of features were observed from the topographs: (i) thick black stripes (also in the X-ray topograph of the GaP substrate) and (ii) a cross-hatched network of narrow straight lines along the [110] and [1-10] crystal directions when the $GaP_{0.98}N_{0.02}$ layer thickness was 600 nm. A few of these straight horizontal lines were also visible in the X-ray topograph of the 225 nm thick $GaP_{0.98}N_{0.02}$ layer.

The thick black lines are images of dislocations in the GaP substrate. Similar dislocations have been observed in the early X-ray topography studies of GaP substrates [50]. The long straight lines, on the other hand, are images of misfit dislocations which originate from the relaxation of the $GaP_{0.98}N_{0.02}$ layer. Similar misfit dislocations have been observed *e.g.,* at GaAsN/GaAs, GaAs/Ge and InGaP/GaAs interfaces [51–54]. Based on the X-ray diffraction topography study it was concluded that the smallest $GaP_{0.98}N_{0.02}$ layer thickness at which misfit dislocations are to form at the GaP/$GaP_{0.98}N_{0.02}$ interface is slightly less than 225 nm. In addition, it was observed that the critical thickness was about four times larger than the value predicted by the Matthews Blakeslee model. Similar discrepency has also been observed from other comparable material combinations as well [52].

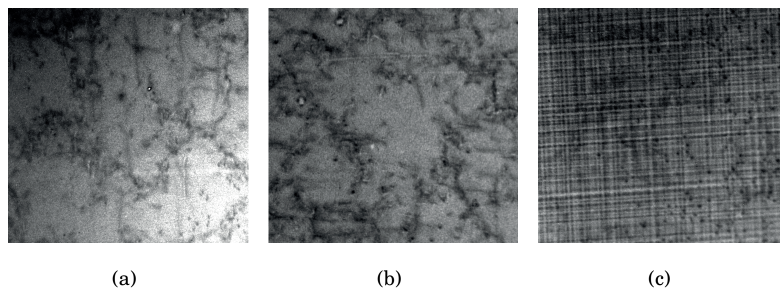

(a) (b) (c)

Figure 6.2. 004 X-ray diffraction topography images of (a) 70 nm thick, (b) 225 nm thick and (c) 600 nm thick $GaP_{0.98}N_{0.02}$ layers on GaP substrate show the formation of misfit dislocations when the layer thickness is larger than 200 nm. The image size corresponds to an area of 1×1 mm^2.

6.1.2 Nitrogen substitutionality in GaPN layers

In Publication VI, nitrogen substitutionality and the formation of point defects in GaPN layers with different nitrogen concentration were characterized by channeling Rutherford backscattering, nuclear reaction analysis and positron annihilation spectroscopy measurements. The nitrogen composition of the layer was varied by changing the DMHy/V ratio in the growth process. It is important to mention that in previous investigations of GaPN alloys no direct measurement of the subsititutional nitrogen content has been performed. The nitrogen content has usually been estimated directly from growth parameters or measured by secondary mass ion spectrometry or high resolution x-ray diffraction (like performed in Publication V). The technique used in Publication VI, *i.e.*, RBS combined with NRA, provides a direct method to estimate the nitrogen configura-

tions in the material [55]. In the following discussion, $GaP_{(1-x)}N_x$ samples are labeled with their overall atomic nitrogen contents of x=1.7%, x=3.6% and x=4.0% obtained from the NRA measurement.

Table 6.1 summarizes the information obtained from the channeling Rutherford backscattering studies and shows that the overall nitrogen content of the GaPN layer increases but similarly the substitutionality of nitrogen into the GaPN layer decreases with increasing DMHy/V ratio. For instance, for the sample with x=1.7% the substitutional fraction of nitrogen, f_{sub}, calculated from both the <100> and <110> channeling direction was very similar which implied that there is no significant amount of interstitial N in this sample. However, for the sample with x=3.6%, the channeling nuclear reaction analysis minimum yield along the <110> direction was allready significantly higher than that from the <100> direction. From this comparison it was estimated that approximately 6% of the nitrogen atoms were in interstitial sites and 68% in substitutional positions. For the x=4% sample, the crystalline quality was too poor to obtain a reasonable estimate of f_{sub}.

The GaPN layer with x=3.6% was grown with the same growth parameters as the thickness series studied in Publication V. Note that the measured nitrogen content of this sample by XRD differed from the results obtained by NRA. This comparison is also shown in Table 6.1 demonstrating that the obtained nitrogen content of x=1.7% and x=3.6% by NRA are larger than that of x=1.1% and x=2.0% obtained by XRD, respectively. However, channeling NRA studies suggested that not all of the nitrogen atoms are in substitutional positions yielding a smaller substitutional composition of x=1.5% and x=2.4% for the nitrogen atoms in the GaPN layer. In addition, it should be noted that the nitrogen content measured by XRD was obtained with Vegard's law from the lattice constant of the layer. It is assumed in Vegard's law that all the atoms are substitutionally incorporated. The most straight forward explanation for the differences between the different measurement methods was that the different nitrogen configurations in the GaPN layer can affect differently to the lattice constant of the layer than that predicted by Vegard's law. This exemplifies the benefits of using channeling RBS measurements combined with NRA studies.

In Publication VI, positron annihilation spectroscopy measurements were also performed to the GaPN layers. This technique showed positron trapping not only in vacancies but also due to nitrogen clusters. Trapping due

Table 6.1. Summary of the channeling RBS and NRA results for the GaPN layers with x=1.7%, x=3.6%, and x=4%. The three rightmost columns show that as the nitrogen content of the layer increases, the fraction of substitutional nitrogen, f_{sub}, decreases and that the fraction of non-substitutional nitrogen (interstitial f_I fraction and random f_{rand} fraction) increases.

DMHy/V ratio	N_{XRD} (%)	N_{NRA} (%)	f_{sub}	f_{rand}	f_I
0.42	1.1	1.7	0.91	0.09	0
0.50	2.0	3.6	0.68	0.26	0.06
0.56	-	4.0	<0.1	>0.85	–

to nitrogen clusters was enhanced with increasing nitrogen content and was not expected based on the positron annihilation spectroscopy results of dilute GaAsN materials [56, 57]. Furthermore, the high magnitude of the effect suggested that multiple N atoms could be present in these positron-trapping centers and was supported by the increased 'random fraction' with nitrogen content observed in the channeling RBS measurements. Previously, the effect of the small impurity atom trapping has been found in, *e.g.*, ZnO with lithium [58, 59].

It was observed that nitrogen incorporation adds many challenges to the growth process compared to the growth of more conventional III-V compound semiconductor alloys. Of these issues, the formation of the misfit dislocation network was expected because nitrogen incorporation adds strain to the epilayer. In addition, the nitrogen incorporation efficiency into the alloy was extremely low. To illustrate how low the incorporation efficiency is, the DMHy/V ratio of 0.5 (*i.e.*, the flow of the nitrogen precursor was the half of the total group V flow) can be compared to the occupation of only 2.4% of the group V sites by nitrogen atoms in the GaPN layer. However, compared to early studies performed to GaAsN and InGaAsN with the same MOVPE apparatus the low nitrogen incorporation was not that suprising [60, 61]. In those studies, the DMHy/V ratio as high as 0.94 resulted in the nitrogen content of 5.6%. However, increasing the DMHy/V ratio larger than 0.6 resulted in an increase in the density of the nitrogen related point defects and the significant degradation of the GaPN layer quality.

Next step would be to perform similar studies for GaAsPN. Note that few GaAsPN layers were already grown for this thesis but no studies were yet performed systematically relating to the factors affecting the material

quality. However, it can be estimated, based on the GaPN results, that the composition of GaAsPN becomes even more challenging to predict because then there exists concentrations of three different group V atoms competing over the occupation of the same lattice sites.

6.1.3 Strain compensation of GaPN layers on silicon

As mentioned earlier, one benefit gained by incorporation of nitrogen into GaP is that it may enable the fabrication of strain compensated layers and devices on silicon substrates. In Publication VII, the nitrogen induced strain compensation was examined by Raman scattering and X-ray diffraction measurements. The 130 nm thick GaPN layer was grown on GaP buffer layer on misoriented silicon substrates. The $GaP_{(1-x)}N_x$ layer composition was estimated from the lattice constant and from the strain state measured by XRD and Raman measurements to be x=1.7%. Note that the substitutional nitrogen content was later verified with RBS measurements combined with NRA to be 2.7%.

The Raman spectra measured from the sample and from a reference GaP buffer layer are shown in Fig. 6.3. The Raman spectra show that the unstressed LO_Γ phonon line of GaP at 403 cm^{-1} shifts between the samples and is observed at 400 cm^{-1} in the GaPN layer and at 404 cm^{-1} in the GaP buffer layer, respectively. The frequency shift of the LO_Γ was attributed to different strain states of the layers and was used to evaluate the strain compensation. The analysis revealed that the strain in the GaPN layer was tensile whereas the GaP buffer layer remained compressively strained. In addition to this, it was observed that the width of the phonon line broadened significantly in the GaPN layer compared to the width of the phonon line in the GaP buffer layer and the shape of the spectrum depended on the used laser wavelength. This was explained by the resonant Raman scattering process which was verified measuring the photoreflectance spectra from the GaPN layer and from the GaP buffer layer. As a result of all the above, it was concluded that the GaPN layer with this composition (*i.e.*, x$\approx$ 2%) is useful for strain compensation. In addition, the results indicated that the GaPN layer possessed an energy state of about 1.9 eV above the valence band maximum, and therefore, the fabricated structure was proposed as a possible structure to be used in the fabrication of intermediate band solar cell. This observations relating to the energy band structure are discussed in more detail in the chapters 6.2 and 7.1.

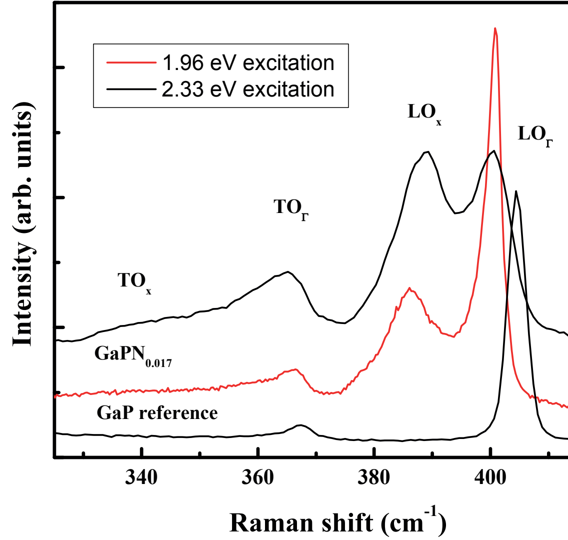

Figure 6.3. Raman spectra of GaPN and GaP layers on silicon substrates.

6.2 Energy band structure of Ga(As)PN

The energy band structure of GaPN was examined by photoluminescence and photoreflectance measurements. Fig. 6.4 shows the PL and PR spectra measured from a $GaP_{0.964}N_{0.036}$ layer. Note that this sample is the same sample showing nitrogen interstitials and other nitrogen related defects in the channeling Rutherford backscattering and nuclear reaction analysis measurements. Low temperature PL spectrum shows a red luminescence from the GaPN layer at 1.9 eV (see inset of Fig. 6.4). In addition, PL peaks at 2.2 eV and 2.15 eV were attributed to donor-acceptor pair related transition and its phonon replica in Publication VI. No PL signal was observed from this sample at room temperature. On the other hand, the room temperature photoreflectance spectrum of the GaPN layer showed three features: (i) a strong transition at 2.78 eV originating from the Γ-point of the GaP substrate, (ii) a photomodulated interference pattern and (iii) a transition from the GaPN layer at 2.07 eV. The photomodulated interference is sometimes observed in PR spectra which can perturbate the line shape of the weak transitions. Due to this issue, it has been addressed in the literature that in these cases it may be more favourable to gather the information by more complex contactless electroreflectance technique [62]. However, the information from the PR spectrum was gath-

ered also from the weak GaPN transition superimposed to the photomodulated interference by fitting a PR curve (red line) to the measured PR spectrum using the Monte-Carlo method described in Chapter 4.4.2.

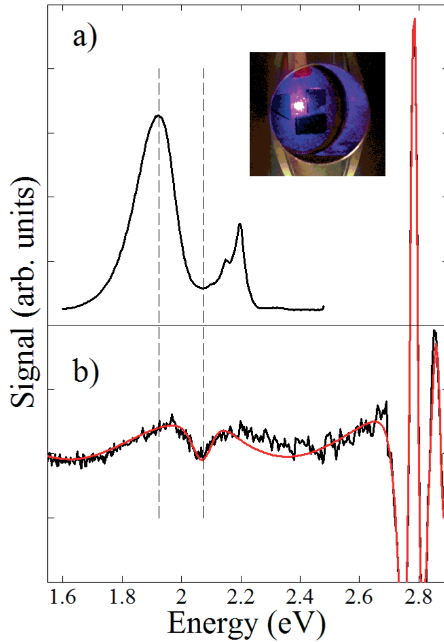

Figure 6.4. (a) Photoluminescence and (b) experimental (black line) and simulated (red line) photoreflectance spectrum of a $GaP_{0.964}N_{0.036}$ layer show transitions from the GaPN layer at different positions. Photoluminecence measurement was carried out at 10 K temperature and photoreflectance at room temperature. The inset shows a photograph of the visible red luminescence.

Fig. 6.4 shows that nitrogen alloying generates red photoluminescence and reveals a direct photoreflectance transition from the $GaP_{0.964}N_{0.036}$ layer below the energy gap of GaP (see Fig. 2.3(b)). This indicates that the nitrogen incorporation transforms the indirect band gap to a pseudo-direct one. The direct nature of the bandgap of GaPN has previously reported by Shan *et al.* [63]. In addition, the location of the transition from $GaP_{0.964}N_{0.036}$ measured by the photoluminescence differs significantly from the critical transition energy measured by photoreflectance. To explain the difference between the PR and PL results it should be noted that the measurement methods measure different things. Photoreflectance signal originates from the critical points of the energy band structure (such as Γ point minimum) which possess large enough density-of-states. Photoluminescence signals, on the other hand, may originate between any two occupied states that have Γ character. For instance,

in nitrogen doped GaP light emitting diodes fabricated in the 1970s, the luminescence was reported to originate between the nitrogen induced impurity states [64, 65]. It should be noted that the nitrogen composition in these LEDs was typically between 10^{18} cm^{-3} to 10^{19} cm^{-3}, and thus, a few orders of magnitude smaller than that in the GaPN layers studied in this thesis. However, the most straightforward explanation for the different locations of photoluminescence and photoreflectance transitions is the photoluminescence signal not originating from a pseudo-direct band-to-band transition visible in PR measurements but instead between the valence band maximum and the energy states of more complex nitrogen configurations. In addition, the shape of the photoluminescence peak (a broad tail at the low energy side) gives further support for this hypothesis.

In Publication VI, it was observed that increasing the nitrogen content redshifts the energy transitions. Similar redshift was also observed with photoreflectance measurements and is in agreement with what previously has been reported in literature [63]. Many models have been developed to explain the effect of nitrogen on the band structure of dilute nitrides. The two-level band anticrossing (BAC) model which includes an anti-crossing interaction between localized nitrogen states and the extended conduction band states of the host material, predicts the bandgap shrinkage and also the splitting of the conduction band of the dilute nitride materials [63, 66]. The conduction band splitting was first observed in GaAsN by electroreflectance [67]. According to the two-level BAC model [68], the coupling between nitrogen states and the host GaP alloy splits the conduction band into two sub-bands

$$E_{\pm}(k) = \frac{1}{2}\left(E_m(k) + E_N \pm \sqrt{(E_m(k) - E_N)^2 + 4[V(x)]^2}\right), \qquad (6.1)$$

where $E_m(k)$ is the dispersion relation of GaP without any nitrogen atoms, E_N=2.19 eV is the energy of the N level, $V(x)$=$C_{m,n}\sqrt{x}$ is the coupling parameter depending on the semiconductor matrix ($C_{m,n}$=3.05 eV for GaPN) and x is the substitutional nitrogen content [63, 69]. It should be noted that despite the capability to predict many of the properties of dilute nitrides, the two-level BAC model is often criticized by theorists. The criticism originates from the experimentally fitted coupling parameter and from the assumption that all nitrogen configurations create an energy level at the same position. For instance, detailed supercell calculations utilizing a pseudopotential method have shown that the states of different nitrogen configurations (*e.g.*, N-N pairs, N triplets) in GaP possess

various energies [70, 71]. In Publication VI, the impact of various nitrogen cluster states was suggested to be the cause for the shape of the photoluminescence peak.

According to the two-level BAC model the conduction band minimum should locate 1.93 eV above the valence band maximum in GaPN with the substitutional nitrogen fraction of x=2.45%. This value agrees with the photoluminescence results but not with the direct transition energy measured by photoreflectance. The difference could be explained by the too large coupling parameter value. Similar issue has previously been discussed in the literature by Harris *et. al.* suggesting that due to the electronegativities and atom sizes of Ga, P and N atoms the coupling parameter should be sligthly smaller than the one in GaAsN which is $C_{m,n}$=1.8 eV [72]. However, it should be noted that the photoreflectance results of GaPN layers grown on silicon substrates agreed better with the two-level BAC model.

The conduction band splitting in GaPN should be observed by the photoreflectance measurements, but it is not. However, this may be explained by the poor sensitivity of the used measurement setup around the 3 eV region where the E_+ band is expected to locate. To demonstrate the conduction band splitting the photoreflectance spectra of a $GaAs_{0.31}P_{0.68}N_{0.01}$ layer is shown in Fig. 6.5. The layer composition was determined by XRD measurements of the quasiforbidden (002) reflection with the method described in Ref. [73]. The photoreflectance spectrum shows transitions from the splitted conduction band at 1.94 eV and 2.44 eV in addition to the transition from the GaP substrate. The energy band structure of the $GaAs_{0.31}P_{0.68}N_{0.01}$ layer calculated according to the two-level BAC model is also visualized in Fig. 6.5. In this model, a parabolic dispersion relation is assumed for the conduction band. In addition, the E_N and $C_{m,n}$ values are linearly interpolated from the values of GaAsN and GaPN. According to the BAC model the E_- and E_+ energy band minima should locate at 1.84 eV and 2.51 eV, respectively, thus agreeing relatively well to the experimentally measured values.

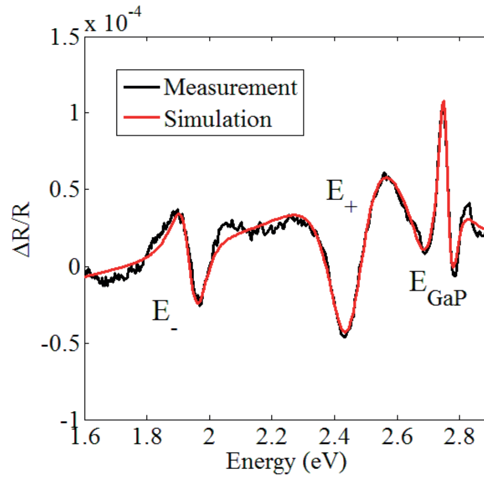

(a)

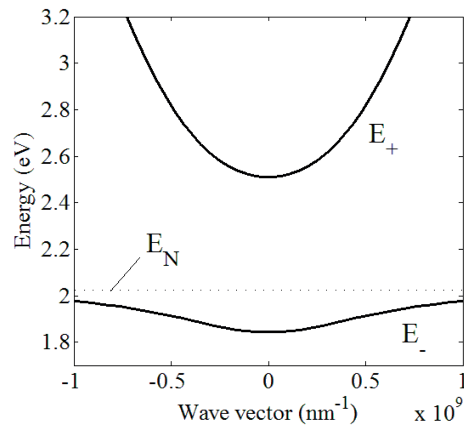

(b)

Figure 6.5. (a) Photoreflectance spectrum of a $GaAs_{0.31}P_{0.68}N_{0.01}$ layer shows the conduction band splitting. (b) The energy band structure calculated according to the two-level BAC model.

7. Properties of the fabricated semiconductor devices that could be integrated on silicon substrate

Heterogeneous integration of III-V compound semiconductors on silicon would allow semiconductor industry to demonstrate many new component designs that could possibly add new functionalities or outperform the current silicon based devices. The proposed components include at least CMOS compatible lasers and LEDs that could be used in on-chip and chip-to-chip communication [10, 19, 74], n-channel high mobility transistors [28], single-transistor dynamic random access memory cells [75] and solar cell devices [4, 5, 76]. This chapter reviews and presents the related research performed for this thesis.

7.1 Use of GaAsPN in silicon based solar cells and intermediate band solar cells

Solar cell industry has made significant investments during the last decades to improve the efficiency of silicon solar cells. The current maximum conversion efficiency of 24.7% has been demonstrated by University of New South Wales [77]. However, it is important to remember that the maximum efficiency is already relatively close to the Schockley-Queisser limit of a silicon solar cell (*i.e.*, 29%).

In a silicon solar cell, like in any other single-junction semiconductor solar cell, the largest efficiency losses originate from the transmission of the sub-bandgap photons through the cell and the incapability to transform all the energy of the absorbed high-energy photons to electricity. Traditionally, this has been addressed by fabricating tandem/multi-junction solar cell devices from materials other than silicon. In these device concepts the absorption spectrum of the device is engineered to better cover the solar spectrum. At the moment, a world record conversion efficiency of 44% has been demonstrated for a triple junction solar cell fabricated

by Spectrolab Inc. However, due to the high material costs required for fabrication of these devices they are typically only used in space applications. Therefore, in order to make solar energy a viable source for large scale energy production in the future, it is more important to increase the efficiency-per-cost ratio, instead of only focusing on the absolute maximum efficiency of the cell. Thus, realization of similar multi junction solar cell devices on low-cost silicon substrates could pave the way for the larger use of solar cells in terrestrial energy harvesting.

GaAsPN material has been proposed to be used in the fabrication of a silicon tandem solar cell with the theoretical maximum efficiency of 50% [49]. In addition, GaAsPN has also been proposed to be used as a material to realize an intermediate band solar cell (IBSC) [78, 79]. The intermediate band solar cell is a semiconductor device in which a light absorbing layer, possessing an energy band between the conduction band and the valence band, is implemented between a single semiconductor *pn*-junction. As a result, three different transitions (*i.e.*, VB->CB, VB->IB and IB->CB) could be utilized in the operation. It has been calculated that the maximum theoretical efficiency for this type of a semiconductor device can be as high as 63.1% with a material having a bandgap of 1.9 eV and the intermediate band locating at 1.2 eV above the valence band edge [80].

The idea to use dilute nitrides in the fabrication of IBSC originates from the splitting of the conduction band [78]. As a matter of fact, it was quite recently demonstrated that an intermediate band solar cell can be fabricated from GaAsN if the energy band lineups are engineered properly [81]. However, it should be noted that the automatically occurring conduction band splitting in dilute nitrides is not enough and that in order to fabricate an intermediate band solar cell from dilute nitrides, the E_- band has to be isolated. This does not happen automatically because the E_- band is the conduction band of the material. In Ref. [81], this issue was solved by engineering the energy band lineups of the device in such a way that a n-type GaAsN layer was connected to a small electron affinity AlGaAs layer. The energy band discontinuity at the n-GaAsN/n-AlGaAs interface forced the E_- energy band to be isolated from the conduction band of the device.

Fig. 7.1 shows the schematic energy band structure of a possible GaAsPN based intermediate band solar cell. The advantages of this design are that the small electron affinity of GaP (*i.e.* 3.8 eV) could potentially isolate the E_- energy band automatically. The first approximation for the conduction

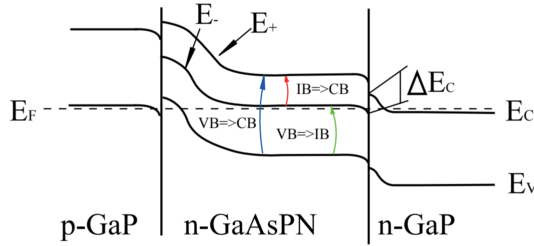

Figure 7.1. Schematics of the energy band structure of GaAsPN intermediate band solar cell.

band discontinuity, ΔE_C, at the semiconductor heterojunction is the difference between the electron affinity of the connected materials, and thus, can be affected by changing the composition of the GaAsPN. In addition, the energy band locations can also similarly be engineered to cover the solar spectrum well, and the strain can be simultaneously compensated because of the quaternary compound.

To examine the absorption properties of GaAsPN based solar cell devices *pn*-diodes were fabricated sandwiching 600 nm thick layers of weakly n-doped and intrinsic $GaAs_{0.31}P_{0.68}N_{0.01}$ between a 500 nm thick p-type GaP layer and a n-type GaP substrate. The doping concentration of the p-type layer was measured by Hall measurement to be $8\times10^{18}/cm^3$. The n-type GaP substrate had a doping concentration (given by the substrate manufactorer) between $2\times10^{17}/cm^3$ and $2\times10^{18}/cm^3$. Backside and frontside ohmic contacts were fabricated from nickel and gold, respectively, and annealed for 10 minutes at 500°C in N_2 atmosphere. In addition, a reference component was fabricated in which a n-doped GaP layer with a doping concentration of $3\times10^{17}/cm^3$ replaced the $GaAs_{0.31}P_{0.68}N_{0.01}$ layer.

To demonstrate that the fabricated devices operate as proper diodes, IV curves of the diodes were measured. Fig. 7.2(a) shows the dark IV curve of the fabricated diode possessing an undoped $GaAs_{0.31}P_{0.68}N_{0.01}$ layer. Despite some leakage current under reverse bias and the traces of series resistance the IV curve clearly shows a rectifying behavior. The IV properties of all the devices were comparable to the presented curve and are, therefore, not shown separately. The leakage current can be partially attributed to the large device area increasing the probability of finding at least a few macroscopic defects. In addition, the leakage currents of GaAsPN diodes can also be partially explained by the strain relaxation caused by the large lattice mismatch between the $GaAs_{0.31}P_{0.68}N_{0.01}$ layer and the GaP substrate. In fact, the surface of the GaAsPN *pn*-diode was

composed of cracks via [110] directions most likely due to the strain relaxation. This issue is illustrated in Fig. 7.2 which shows a photograph of the surface of the fabricated component. The formation of misfit dislocations can be predicted to occur when the layer thickness is larger than 50 nm according to the discussion relating to the Matthews Blakeslee model presented in Chapter 6.1.1. Therefore, the strain relaxation is not suprising as the thickness of the GaAsPN layer was 600 nm. In order to prevent the formation of misfit dislocations and the presence of cracks on the component surface and to grow a device only consisting of pseudomorphic layers, more nitrogen should be incorporated in the $GaAs_{0.31}P_{0.68}N_{0.01}$ layer. This could be performed by increasing the DMHy/V ratio, but as was explained in Chapter 6.1.2., at the same time the nitrogen substitutionality could be predicted to decrease and the density of nitrogen related point defects to increase. It is well known that these nitrogen related point defects reduce the lifetime of charge carriers, and therefore, most likely degrade the operation of the devices such as solar cells. Based on this discussion, further optimization related to finding a more optimal growth parameters for the GaAsPN layer is still required in addition to performing similar structural studies as presented in Chapter 6.

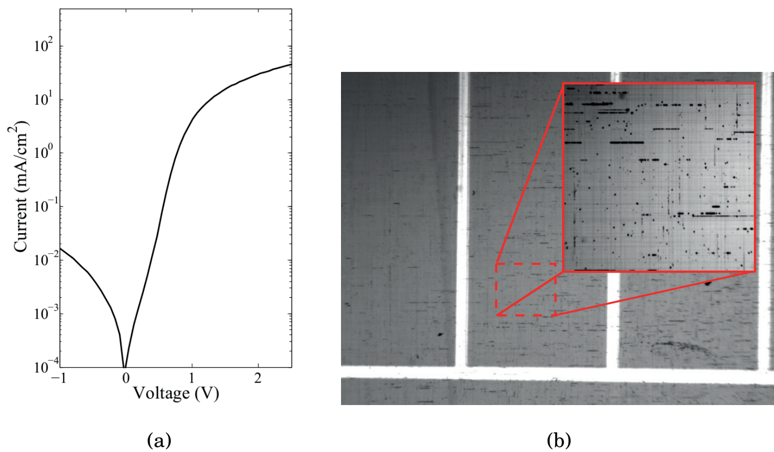

Figure 7.2. (a) Dark IV curve of the fabricated pn diode possessing an intrinsic $GaAs_{0.31}P_{0.68}N_{0.01}$ layer inside the pn-junction. (b) Photograph of the fabricated diode shows the cracking of the component due to the strain. The white lines are the top Au/Al contacts with the width of 100μm.

Fig. 7.3 shows the photocurrent response of the fabricated devices. The photoreflectance spectrum of the $GaAs_{0.31}P_{0.68}N_{0.01}$ layer is also shown for comparison. Two peaks can be observed in the photocurrent spectrum agreeing with the E_+ and E_- transitions relatively well. The magnitude

of the E_- transition is influenced by the $GaAs_{0.31}P_{0.68}N_{0.01}$ layer doping. On the other hand, the photocurrent spectrum of the reference diode possesses the features typical to the absorption spectrum of GaP. The photocurrent is created at an energy larger than the indirect band gap of GaP located at 2.27 eV and becomes larger at energies closer to the direct band gap of GaP. As mentioned earlier in this chapter, an optimal material combined to a silicon solar cell for the fabrication of a tandem cell would possess an energy gap of 1.8 eV [80]. The fabricated GaAsPN based devices have an energy gap of 1.94 eV based on photoreflectance measurements agreeing relatively well with the desired value. In addition, the absorption spectrum of the diode possessing an undoped $GaAs_{0.31}P_{0.68}N_{0.01}$ layer is relatively broad which is due to the small separation between the E_- and E_+ energy states. This suggests that from the absorption perspective this material could be well used in the fabrication of a silicon based tandem solar cell. However, it should be noted that if the fabricated device would operate as an IBSC the photocurrent should preferably be only observed at energies larger than the E_+ transition. The fact that photocurrent is also created by the photons with energies corresponding to the E_- transition suggests that the energy band discontinuity at the $GaAs_{0.31}P_{0.68}N_{0.01}$/GaP interface is not enough to isolate the E_-. However, for the diode possessing a weakly n-doped $GaAs_{0.31}P_{0.68}N_{0.01}$ the relative magnitude of the photocurrent signal is weaker at energies corresponding to the E_- transition. This could suggest that the E_- band is at least partially isolated. However, further studies are required to make a definite conclusion.

7.2 GaAs MIS structures

High mobility GaAs based metal insulator semiconductor (MIS) capacitors could be used in the fabrication of III-V metal-oxide-semiconductor field-effect transistors (MOSFET). Recently, this topic has been of interest for the silicon integrated circuit industry because the limits of down scaling are approaching. The benefit of using high mobility channel materials in CMOS technology is that the high mobility provides a mean to enhance the operation of CMOS chips as down scaling continues because it hinders the occurrence of many short-channel effects present in the future transistor nodes. Lately, the utilization of high mobility III-V compound semiconductors (and germanium) in the IC technology has

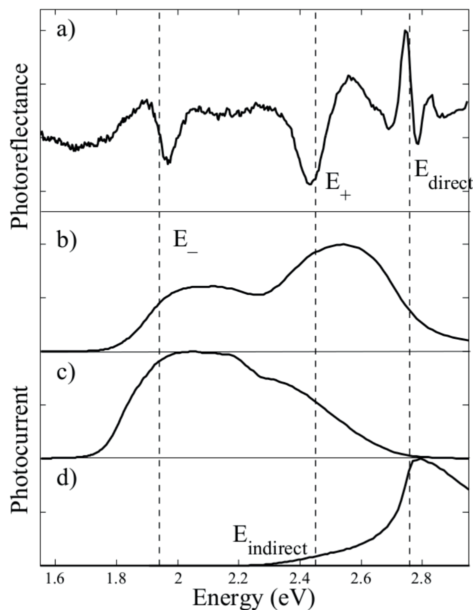

Figure 7.3. Comparison between (a) photoreflectance of the $GaAs_{0.31}P_{0.68}N_{0.01}$ layer and (b-d) photocurrent spectra of the fabricated *pn*-diodes. The light absorbing layer sandwiched between the *pn*-junction is (b) n-doped $GaAs_{0.31}P_{0.68}N_{0.01}$ layer, (c) intrinsic $GaAs_{0.31}P_{0.68}N_{0.01}$ layer and (d) n-GaP layer.

even been included in the international technology roadmap for semiconductors (ITRS) as an alternative channel materials to continue to improve the circuit performance [6]. In the 2012 edition of the ITRS, it was predicted that the first semiconductor company could bring the high mobility materials to the production level in 2019.

Electron mobility of GaAs is six times larger than that of silicon and can be increased even further by alloying GaAs with indium. As a result, integration of these III-V compound materials on silicon can enhance the component performance significantly. The most typically proposed integration scheme is the wafer bonding. However, it should be noted that the monolithic integration of GaAs and germanium is already reality in the fabrication of commercial multijunction solar cells. In addition to this, there exists at the moment silicon on insulator wafers in which a strain free germanium layer has been deposited locally in the device layer [82]. This combination of materials (*i.e.*, GaAs on Ge) would be almost optimal from the charge carrier mobility point of view due to the high hole-mobility of germanium (see Table 2.1). Furthermore, GaAs layers have been grown monolithically [22] and GaAs nanowires by the VLS fabrication method directly on silicon substrates (see chapter 5.3 or *e.g.* Ref.

[83]). However, integration of GaAs in the silicon technology is still far from the stage required for commercialization.

For a long time, the missing block to fabricate a high quality MOSFET from GaAs (and practically from any III-V material) has been the lack of an insulator material which would allow forming interfaces with quality comparable to the Si/SiO_2 system. However, due to atomic layer deposition (ALD) a vast number of new insulator materials is available almost on any substrates. As a result, there has been an increasing number of reports in the literature focusing on the III-V/insulator interface quality [84–87]. The most important requirements for the insulator layer for the fabrication of a high-quality MOSFET are thermal stability, high dielectric constant with sufficient band offsets, the formation of a high-quality interface with a low interface trap density and an unpinned Fermi level. Fermi level pinning means that the Fermi level is fixed at a specific energy of the semiconductor/insulator interface. This prevents the transistor from switching between the different states. Fermi level pinning is commonly attributed to the unpassivated dangling bonds which exist on the GaAs surface after the formation of the native oxide.

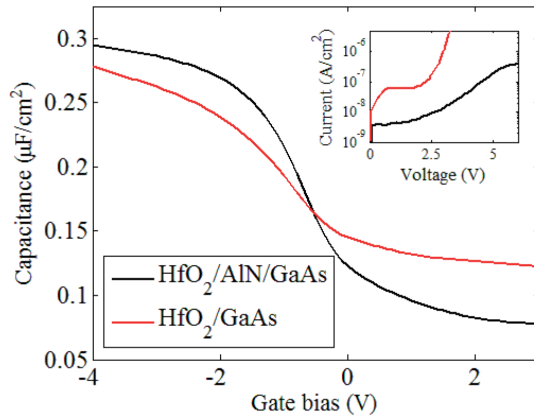

Figure 7.4. Capacitance-voltage curves of a HfO_2/AlN/GaAs MIS capacitor (black line) and a HfO_2/GaAs Mis capacitor (red line). Inset shows the IV-curve of the MIS capacitors.

In Publication VIII, the HfO_2/AlN/GaAs interface was studied and high-k GaAs MIS capacitors with an unpinned Fermi level were fabricated. AlN layer with a thickness of 2 nm was deposited to passivate the dangling bonds at the interface. Both the AlN and a 35 nm thick HfO_2 layers were deposited by ALD, (more information about the ALD fabrication can be found in Refs. [88, 89]). The Fermi level unpinning was shown by

capacitance-voltage (CV) and current-voltage (IV) measurements. Fig. 7.4 shows typical CV curves measured from a HfO_2/AlN/GaAs and a HfO_2/GaAs reference MIS capacitors. It can be observed that the AlN passivation layer enables a larger change in circuit capacitance which suggests better interface quality. In Publication VIII, the capacitance was tied up to the band bending of 1.2 eV, and therefore, an unpinned Fermi level was concluded. The observation was supported by illumination and temperature induced effects preventing the deep depletion operating mode. In addition, the amorphous AlN layer improves the electrical quality of the HfO_2 layer. This was observed from the IV curves of the MIS capacitors (inset of Fig. 7.4) which show a significantly larger leakage current for the HfO_2/GaAs MIS capacitors.

Results demonstrate that unpinned Fermi level can be achieved when AlN passivation layer is deposited on GaAs surface. Next step would be to fabricate MOSFET devices from Au/HfO_2/AlN gate stacks and to study their operation. This was not performed because the fabrication process for source and drain regions is more difficult than that used in silicon CMOS industry because ion implantation is not that straight forward for III-V compound semiconductors. In addition, ALD process for AlN deposition could still be optimized further.

8. Summary

Integration of GaAsP based III-V compound semiconductors on silicon was studied in this thesis. The integration concepts used were the monolithic growth of GaP on silicon and GaAs nanowire growth via VLS growth method. All the samples were fabricated by metalorganic vapor phase epitaxy. AFM studies of the monolithically grown GaP layers showed that the growth of GaP needs to be started at low temperatures to obtain a layer-by-layer growth mode. In addition, it was observed that careful preparation of the silicon substrate prior to the epitaxial growth was crucial to obtain high-quality layers. For instance, transverse scan analysis in addition to AFM revealed the existence of antiphase domains in GaP layers on exactly oriented silicon substrates. In addition, threading dislocation and stacking fault defects most likely affected the broadening of the transverse scan line profiles of GaP layers on misoriented silicon substrates.

The crystallinity of GaAs nanowires grown on glass and silicon substrates, and AZO layers on silicon by the VLS method were examined by powder XRD measurements. GaAs nanowires were crystallized in the zinc-blende crystal structure and it was observed that the VLS growth method enables the fabrication of GaAs nanowires on silicon and even on amorphous substrates. The powder XRD studies were combined with the transmission electron microscopy examinations. The results from both of the methods agreed and revealed extremely detailed information from single wires as well as more statistical analysis throughout the whole sample. In addition, photoluminescence measurements implied that the optical properties of GaAs nanowires were better when grown on AZO layers on silicon and glass substrates than on silicon substrates. It was speculated that this may be related to the presence of some impurity atoms (*e.g.*, zinc) in the growth process.

The growth and characterization of Ga(As)PN alloys, with the compo-

sition nearly lattice-matched to silicon, was examined by X-ray topography, Rutherford backscattering spectroscopy, nuclear reaction analysis and positron annihilation spectroscopy measurements. In these studies, GaPN layers were grown directly on GaP substrates to rule out the factors arising from the GaP/silicon interface. It was observed that nitrogen incorporation adds many challenges to the growth process. Of these issues, the formation of the misfit dislocation network was expected because nitrogen incorporation adds strain to the epilayer. The critical thickness for the formation of the misfit dislocation network for the $GaP_{0.98}N_{0.02}$ alloy on GaP substrate was about 200 nm. In addition, the nitrogen incorporation efficiency was observed to be extremely low. It was observed that increasing the DMHy/V ratio increased the nitrogen content as well as the density of the nitrogen related point defects and cluster states in the GaPN alloy. The results relating to the strain state and also the energy band structure of GaPN layers grown on silicon were discussed. Raman scattering and X-ray diffraction measurements implied that the nitrogen incorporation enables the fabrication of strain compensated GaP based structures on silicon substrates.

The effect of nitrogen incorporation on the energy band structure of Ga(As)PN was studied by photoluminescence and photoreflectance measurements. The different locations for the photoluminescence and photoreflectance transitions of the GaPN layer implied that the measurement methods measure different transitions. It was suggested that the photoluminescence signal instead of originating from a direct band-to-band transition was originating from the states related to nitrogen clusters. Furthermore, the photoreflectance measurements revealed the conduction band splitting in GaAsPN alloys.

Aforementioned studies relating to the material properties of GaAsPN layers were performed to gather information for monolithical integration of compound semiconductor devices on low cost silicon substrates. Among these devices, an IBSC device and tandem solar cells fabricated from GaAsPN materials were discussed. *pn*-diodes fabricated from this material were chracterized electrically and spectrally. The photocurrent spectra revealed transitions from E_- and E_+ energy bands and the use of this type of structure in tandem and intermediate band solar cells was discussed. Further work relating to the material growth is still required to find a mean to enhance the overall quality of the material and to compensate the lattice strain more effectively by incorporating more nitrogen

into the GaAsPN alloy.

The surface passivation of GaAs was studied for the fabrication of monolithically integrated high mobility transistor structures. The examinations were performed fabricating high-k MIS capacitors from GaAs with an insulator stack comprising an AlN layer and a high-k HfO_2 layer. The AlN layer was deposited to passivate the dangling bonds at the GaAs surface. The Fermi level unpinning was shown by capacitance-voltage and current-voltage measurements. The change in circuit capacitance corresponded to the maximum band bending of 1.2 eV. The Fermi-level unpinning was supported by the observation of the illumination and temperature induced effects preventing the deep depletion operating mode. In addition, it was observed that the amorphous nature of the AlN layer improved the electrical quality of the HfO_2 layer showing significantly smaller leakage current when the AlN layer was present. Next step would be to fabricate MOSFET devices from Au/HfO_2/AlN gate stacks and to study their operation.

As addressed many times in this thesis, semiconductor research community attempts to constantly integrate different materials on silicon substrates. These materials could add new functionalities, and thus, enhance the operation of many semiconductor devices. As a result, integration of III-V compound semiconductors on silicon will provide new tools for component designers due to many different properties of III-V compound materials listed in this thesis. However, in this discussion it is important to remember, whether the integration will be performed via the monolithic approach, the VLS growth mechanism or some other technique, there still exists many challenges some of which described in this thesis that have to overcome to make the integration a standard process for the semiconductor industry.

Bibliography

[1] G. Moore, “Cramming more components onto integrated circuits,” *Electronics*, vol. 38, no. 8, 1965.

[2] D. Liang and J. E. Bowers, “Recent progress in lasers on silicon,” *Nature Photonics*, vol. 4, no. 8, pp. 511–517, 2010.

[3] R. Soref, “The past, present, and future of silicon photonics,” *IEEE Journal of Selected Topics in Quantum Electronics*, vol. 12, no. 6, pp. 1678–1687, 2006.

[4] J. R. Lang, J. Faucher, S. Tomasulo, K. N. Yaung, and M. L. Lee, “Comparison of GaAsP solar cells on GaP and GaP/Si,” *Applied Physics Letters*, vol. 103, no. 9, p. 092102, 2013.

[5] T. Grassman, A. Carlin, and S. Ringel, “Metamorphic GaAsP and InGaP photovoltaic materials on Si for high-efficiency III-V/Si multijunction solar cells,” in *35th IEEE Photovoltaic Specialists Conference (PVSC)*, 2010, pp. 002 029–002 033.

[6] *International Technology Roadmap for Semiconductors*, 2012.

[7] T. J. Grassman, M. R. Brenner, S. Rajagopalan, R. Unocic, R. Dehoff, M. Mills, H. Fraser, and S. A. Ringel, “Control and elimination of nucleation-related defects in GaP/Si (001) heteroepitaxy,” *Applied Physics Letters*, vol. 94, no. 23, p. 232106, 2009.

[8] K. Volz, A. Beyer, W. Witte, J. Ohlmann, I. Nemeth, B. Kunert, and W. Stolz, “GaP-nucleation on exact Si (001) substrates for III/V device integration,” *Journal of Crystal Growth*, vol. 315, no. 1, pp. 37 – 47, 2011.

[9] T. J. Grassman, J. A. Carlin, B. Galiana, L.-M. Yang, F. Yang, M. J. Mills, and S. A. Ringel, “Nucleation-related defect-free GaP/Si(100) heteroepitaxy via metal-organic chemical vapor deposition,” *Applied Physics Letters*, vol. 102, no. 14, p. 142102, 2013.

[10] S. Liebich, M. Zimprich, A. Beyer, C. Lange, D. J. Franzbach, S. Chatterjee, N. Hossain, S. J. Sweeney, K. Volz, B. Kunert, and W. Stolz, “Laser operation of Ga(NAsP) lattice-matched to (001) silicon substrate,” *Applied Physics Letters*, vol. 99, no. 7, p. 071109, 2011.

[11] J. R. Reboul, L. Cerutti, J. B. Rodriguez, P. Grech, and E. Tournié, “Continuous-wave operation above room temperature of GaSb-based laser diodes grown on Si,” *Applied Physics Letters*, vol. 99, no. 12, p. 121113, 2011.

[12] B. E. Warren, *X-Ray diffraction*. Addison-Wesley, 1969.

[13] A. Létoublon, W. Guo, C. Cornet, A. Boulle, M. Véron, A. Bondi, O. Durand, T. Rohel, O. Dehaese, N. Chevalier, N. Bertru, and A. L. Corre, “X-ray study of antiphase domains and their stability in MBE grown GaP on Si,” *Journal of Crystal Growth*, vol. 323, no. 1, pp. 409 – 412, 2011.

[14] T. Tuomi, “Synchrotron X-ray topography of electronic materials,” *Journal of Synchrotron Radiation*, vol. 9, no. 3, pp. 174–178, May 2002.

[15] M. Mayer, “SIMNRA, a simulation program for the analysis of NRA, RBS and ERDA,” *AIP Conference Proceedings*, vol. 475, no. 1, pp. 541–544, 1999.

[16] D. E. Aspnes, “Direct verification of the third-derivative nature of electroreflectance spectra,” *Physical Review Letters*, vol. 28, pp. 168–171, Jan 1972.

[17] E. Nicollian and J. Brews, *MOS (Metal-oxide-semiconductor) Physics and Technology*. John Wiley & Sons, Inc., 1982.

[18] R. Engel-Herbert, Y. Hwang, and S. Stemmer, “Comparison of methods to quantify interface trap densities at dielectric/III-V semiconductor interfaces,” *Journal of Applied Physics.*, vol. 108, no. 12, p. 124101, 2010.

[19] O. Vendier, S. W. Bond, M. Lee, S. Jung, M. Brooke, N. Jokerst, and R. P. Leavitt, “Stacked silicon CMOS circuits with a 40-Mb/s through-silicon optical interconnect,” *IEEE Photonics Technology Letters*, vol. 10, no. 4, pp. 606–608, 1998.

[20] D. L. Mathine, “The integration of III-V optoelectronics with silicon circuitry,” *IEEE Journal of Selected Topics in Quantum Electronics*, vol. 3, no. 3, pp. 952–959, 1997.

[21] A. Dadgar, F. Schulze, M. Wienecke, A. Gadanecz, J. Bläsing, P. Veit, T. Hempel, A. Diez, J. Christen, and A. Krost, “Epitaxy of GaN on silicon—impact of symmetry and surface reconstruction,” *New Journal of Physics*, vol. 9, no. 10, p. 389, 2007.

[22] S. F. Fang, K. Adomi, S. Iyer, H. Morkoç, H. Zabel, C. Choi, and N. Otsuka, “Gallium arsenide and other compound semiconductors on silicon,” *Journal of Applied Physics*, vol. 68, no. 7, pp. R31–R58, 1990.

[23] B.-Y. Tsaur and G. M. Metze, “Molecular beam epitaxy of GaAs and AlGaAs on Si,” *Applied Physics Letters*, vol. 45, no. 5, pp. 535–536, 1984.

[24] P. Caroff, M. Jeppsson, D. Wheeler, M. Keplinger, B. Mandl, J. Stangl, A. Seabaugh, G. Bauer, and L.-E. Wernersson, “InAs film grown on Si (111) by metal organic vapor phase epitaxy,” *Journal of Physics: Conference Series*, vol. 100, no. 4, p. 042017, 2008.

[25] D. Wuu, R. H. Horng, K. C. Huang, and M. Lee, “Improvements in the organometallic heteroepitaxy of indium phosphide directly on silicon,” *Applied Physics Letters*, vol. 54, no. 3, pp. 236–238, 1989.

[26] Y. Kim, Y. Noh, M. Kim, J. Oh, and K. Chung, “Transmission electron microscopy study of the initial growth stage of GaSb grown on Si (001) substrate by molecular beam epitaxy method,” *Thin Solid Films*, vol. 518, no. 8, pp. 2280 – 2284, 2010.

[27] Y. Song and M. Larry Lee, "InGaAs/GaP quantum dot light-emitting diodes on Si," *Applied Physics Letters*, vol. 103, no. 14, p. 141906, 2013.

[28] L. Desplanque, S. E. Kazzi, C. Coinon, S. Ziegler, B. Kunert, A. Beyer, K. Volz, W. Stolz, Y. Wang, P. Ruterana, and X. Wallart, "Monolithic integration of high electron mobility InAs-based heterostructure on exact (001) silicon using a GaSb/GaP accommodation layer," *Applied Physics Letters*, vol. 101, no. 14, p. 142111, 2012.

[29] Z. Wang, C. Junesand, W. Metaferia, C. Hu, L. Wosinski, and S. Lourdudoss, "III–Vs on Si for photonic applications—a monolithic approach," *Materials Science and Engineering: B*, vol. 177, no. 17, pp. 1551 – 1557, 2012.

[30] V. Lehmann, K. Mitani, R. Stengl, T. Mii, and U. Gösele, "Bubble-free wafer bonding of GaAs and InP on silicon in a microcleanroom," *Japanese Journal of Applied Physics*, vol. 28, no. Part 2, No. 12, pp. L2141–L2143, 1989.

[31] O. Parillaud, E. Gil Lafon, B. Gérard, P. Etienne, and D. Pribat, "High quality InP on Si by conformal growth," *Applied Physics Letters*, vol. 68, no. 19, pp. 2654–2656, 1996.

[32] D. Pribat, B. Gerard, M. Dupuy, and P. Legagneux, "High quality GaAs on Si by conformal growth," *Applied Physics Letters*, vol. 60, no. 17, pp. 2144–2146, 1992.

[33] W. Ju, D. A. Gulino, and R. Higgins, "Epitaxial lateral overgrowth of gallium nitride on silicon substrate," *Journal of Crystal Growth*, vol. 263, no. 1–4, pp. 30 – 34, 2004.

[34] R. S. Wagner and W. C. Ellis, "Vapor-liquid-solid mechanism of single crystal growth," *Applied Physics Letters*, vol. 4, no. 5, pp. 89–90, 1964.

[35] H. Shtrikman, R. Popovitz-Biro, A. Kretinin, and M. Heiblum, "Stacking-faults-free zinc blende GaAs nanowires," *Nano Letters*, vol. 9, no. 1, pp. 215–219, 2009.

[36] Z. Cui, T. Ishikura, F. Jabeen, J.-C. Harmand, and K. Yoh, "Fabrication and characterization of a δ-doped InAs/InP core shell nanowire transistor," *Journal of Crystal Growth*, vol. 378, no. 0, pp. 511 – 514, 2013.

[37] J. Wallentin, N. Anttu, D. Asoli, M. Huffman, I. Aberg, M. H. Magnusson, G. Siefer, P. Fuss-Kailuweit, F. Dimroth, B. Witzigmann, H. Q. Xu, L. Samuelson, K. Deppert, and M. T. Borgstrom, "InP nanowire array solar cells achieving 13.8 efficiency by exceeding the ray optics limit," *Science*, vol. 339, no. 6123, pp. 1057–1060, 2013.

[38] Y. Takagi, Y. Furukawa, A. Wakahara, and H. Kan, "Lattice relaxation process and crystallographic tilt in GaP layers grown on misoriented Si (001) substrates by metalorganic vapor phase epitaxy," *Journal of Applied Physics*, vol. 107, no. 6, p. 063506, 2010.

[39] I. Nemeth, B. Kunert, W. Stolz, and K. Volz, "Heteroepitaxy of GaP on Si: Correlation of morphology, anti-phase-domain structure and MOVPE growth conditions," *Journal of Crystal Growth*, vol. 310, no. 7-9, pp. 1595 – 1601, 2008.

[40] B. Kunert, I. Nemeth, S. Reinhard, K. Volz, and W. Stolz, “Si (001) surface preparation for the antiphase domain free heteroepitaxial growth of GaP on Si substrate,” *Thin Solid Films*, vol. 517, no. 1, pp. 140 – 143, 2008.

[41] J. Gowers, “TEM image contrast from antiphase domains in GaAs: Ge(001) grown by MBE,” *Applied Physics A*, vol. 34, no. 4, pp. 231–236, 1984.

[42] O. Durand, A. Létoublon, D. Rogers, and F. H. Teherani, “Interpretation of the two-components observed in high resolution x-ray diffraction ω scan peaks for mosaic ZnO thin films grown on c-sapphire substrates using pulsed laser deposition,” *Thin Solid Films*, vol. 519, no. 19, pp. 6369 – 6373, 2011.

[43] A. Gibaud, R. A. Cowley, D. F. McMorrow, R. C. C. Ward, and M. R. Wells, “High-resolution x-ray-scattering study of the structure of niobium thin films on sapphire,” *Physical Review B*, vol. 48, pp. 14 463–14 471, 1993.

[44] P. F. Miceli, J. Weatherwax, T. Krentsel, and C. J. Palmstrom, “Specular and diffuse reflectivity from thin films containing misfit dislocations,” *Physica B: Condensed Matter*, vol. 221, no. 1-4, pp. 230 – 234, 1996.

[45] P. F. Miceli and C. J. Palmstrom, “X-ray scattering from rotational disorder in epitaxial films: An unconventional mosaic crystal,” *Physical Review B*, vol. 51, pp. 5506–5509, 1995.

[46] V. M. Kaganer, O. Brandt, H. Riechert, and K. K. Sabelfeld, “X-ray diffraction of epitaxial films with arbitrarily correlated dislocations: Monte Carlo calculation and experiment,” *Physical Review B*, vol. 80, p. 033306, Jul 2009.

[47] M. Mattila, T. Hakkarainen, H. Jiang, E. I. Kauppinen, and H. Lipsanen, “Effect of substrate orientation on the catalyst-free growth of InP nanowires,” *Nanotechnology*, vol. 18, no. 15, p. 155301, 2007.

[48] B. Kunert, S. Zinnkann, K. Volz, and W. Stolz, “Monolithic integration of Ga(NAsP)/(BGa)P multi-quantum well structures on (001) silicon substrate by MOVPE,” *Journal of Crystal Growth*, vol. 310, no. 23, pp. 4776 – 4779, 2008.

[49] S. Almosni, C. Robert, T. N. Thanh, C. Cornet, A. Létoublon, T. Quinci, C. Levallois, M. Perrin, J. Kuyyalil, L. Pedesseau, A. Balocchi, P. Barate, J. Even, J. M. Jancu, N. Bertru, X. Marie, O. Durand, and A. L. Corre, “Evaluation of InGaPN and GaAsPN materials lattice-matched to Si for multi-junction solar cells,” *Journal of Applied Physics*, vol. 113, no. 12, p. 123509, 2013.

[50] J. Hilgarth, “Direct observation of dislocations in GaP crystals,” *Journal of Materials Science*, vol. 13, pp. 2697–2702, 1978.

[51] A. Lankinen, L. Knuuttila, T. Tuomi, P. Kostamo, A. Saynatjoki, J. Riikonen, H. Lipsanen, P. McNally, X. Lu, H. Sipila, S. Vaijarvi, and D. Lumb, “Synchrotron X-ray topography study of defects in epitaxial GaAs on high-quality Ge,” *Nuclear Instruments and Methods in Physics Research Section A: Accelerators, Spectrometers, Detectors and Associated Equipment*, vol. 563, no. 1, pp. 62 – 65, 2006.

[52] A. Lankinen, L. Knuuttila, P. Kostamo, T. Tuomi, H. Lipsanen, P. McNally, and L. O'Reilly, "Synchrotron topography and X-ray diffraction study of GaInP layers grown on GaAs/Ge," *Journal of Crystal Growth*, vol. 311, no. 22, pp. 4619 – 4627, 2009.

[53] J. Toivonen, T. Tuomi, J. Riikonen, L. Knuuttila, T. Hakkarainen, M. Sopanen, H. Lipsanen, P. McNally, W. Chen, and D. Lowney, "Misfit dislocations in GaAsN/GaAs interface," *Journal of Materials Science: Materials in Electronics*, vol. 14, pp. 267–270, 2003.

[54] O. Reentilä, A. Lankinen, M. Mattila, A. Säynätjoki, T. Tuomi, H. Lipsanen, L. O'Reilly, and P. McNally, "In-situ optical reflectance and synchrotron x-ray topography study of defects in epitaxial dilute GaAsN on GaAs," *Journal of Materials Science: Materials in Electronics*, vol. 19, pp. 137–142, 2008.

[55] L. Feldman, J. W. Mayer, and S. T. Picraux, *Materials Analysis by Ion Channeling*. Academic, New York, 1982.

[56] J. Toivonen, T. Hakkarainen, M. Sopanen, H. Lipsanen, J. Oila, and K. Saarinen, "Observation of defect complexes containing Ga vacancies in GaAsN," *Applied Physics Letters*, vol. 82, no. 1, pp. 40–42, 2003.

[57] J. Slotte, K. Saarinen, E.-M. Pavelescu, T. Hakkarainen, and M. Pessa, "Nitrogen related vacancies in GaAs based quantum well superlattices," *Applied Physics Letters*, vol. 89, no. 6, p. 061903, 2006.

[58] K. M. Johansen, A. Zubiaga, F. Tuomisto, E. V. Monakhov, A. Y. Kuznetsov, and B. G. Svensson, "H passivation of Li on Zn-site in ZnO: Positron annihilation spectroscopy and secondary ion mass spectrometry," *Physical Review B*, vol. 84, p. 115203, 2011.

[59] K. M. Johansen, A. Zubiaga, I. Makkonen, F. Tuomisto, P. T. Neuvonen, K. E. Knutsen, E. V. Monakhov, A. Y. Kuznetsov, and B. G. Svensson, "Identification of substitutional Li in n-type ZnO and its role as an acceptor," *Physical Review B*, vol. 83, p. 245208, 2011.

[60] J. Toivonen, T. Hakkarainen, M. Sopanen, and H. Lipsanen, "High nitrogen composition GaAsN by atmospheric pressure metalorganic vapor-phase epitaxy," *Journal of Crystal Growth*, vol. 221, no. 1–4, pp. 456 – 460, 2000.

[61] T. Hakkarainen, J. Toivonen, H. Koskenvaara, M. Sopanen, and H. Lipsanen, "Structural and optical properties of GaInNAs/GaAs quantum structures," *Journal of Physics: Condensed Matter*, vol. 16, no. 31, p. S3009, 2004.

[62] R. Kudrawiec, P. Sitarek, J. Misiewicz, S. R. Bank, H. B. Yuen, M. A. Wistey, and J. S. Harris, "Interference effects in electromodulation spectroscopy applied to GaAs-based structures: A comparison of photoreflectance and contactless electroreflectance," *Applied Physics Letters*, vol. 86, no. 9, p. 091115, 2005.

[63] W. Shan, W. Walukiewicz, K. M. Yu, J. Wu, J. W. Ager, E. E. Haller, H. P. Xin, and C. W. Tu, "Nature of the fundamental band gap in GaNP alloys," *Applied Physics Letters*, vol. 76, no. 22, pp. 3251–3253, 2000.

[64] D. G. Thomas, J. J. Hopfield, and C. J. Frosch, "Isoelectronic traps due to nitrogen in gallium phosphide," *Physical Review Letters*, vol. 15, pp. 857–860, 1965.

[65] B. Gil, J. Camassel, J. P. Albert, and H. Mathieu, “Local symmetry of nitrogen pairs in GaP,” *Physical Review B*, vol. 33, pp. 2690–2700, 1986.

[66] W. Walukiewicz, W. Shan, K. M. Yu, J. W. Ager, E. E. Haller, I. Miotkowski, M. J. Seong, H. Alawadhi, and A. K. Ramdas, “Interaction of localized electronic states with the conduction band: Band anticrossing in II-VI semiconductor ternaries,” *Physical Review Letters*, vol. 85, pp. 1552–1555, 2000.

[67] J. D. Perkins, A. Mascarenhas, Y. Zhang, J. F. Geisz, D. J. Friedman, J. M. Olson, and S. R. Kurtz, “Nitrogen-activated transitions, level repulsion, and band gap reduction in $GaAs_{(1-x)}N_x$ with x<0.03,” *Physical Review Letters*, vol. 82, pp. 3312–3315, 1999.

[68] J. Wu, W. Walukiewicz, K. M. Yu, J. W. Ager, E. E. Haller, Y. G. Hong, H. P. Xin, and C. W. Tu, “Band anticrossing in GaPN alloys,” *Physical Review B*, vol. 65, p. 241303, 2002.

[69] W. Shan, W. Walukiewicz, J. W. Ager, E. E. Haller, J. F. Geisz, D. J. Friedman, J. M. Olson, and S. R. Kurtz, “Band anticrossing in GaInNAs alloys,” *Physical Review Letters*, vol. 82, pp. 1221–1224, 1999.

[70] P. R. C. Kent and A. Zunger, “Theory of electronic structure evolution in GaAsN and GaPN alloys,” *Physical Review B*, vol. 64, p. 115208, 2001.

[71] S. V. Dudiy, P. R. C. Kent, and A. Zunger, “Penetration of electronic perturbations of dilute nitrogen impurities deep into the conduction band of GaPN,” *Physical Review B*, vol. 70, p. 161304, 2004.

[72] C. Harris, A. Lindsay, and E. P. O’Reilly, “Evolution of N defect states and optical transitions in ordered and disordered GaPN alloys,” *Journal of Physics: Condensed Matter*, vol. 20, no. 29, p. 295211, 2008.

[73] J. Tilli, H. Jussila, K. Yu, T. Huhtio, and M. Sopanen, “Composition determination of quaternary GaAsPN layers from single XRD measurement of quasi-forbidden (002) reflection,” *Journal of Applied Physics*, vol. 115, p. 203102, 2014.

[74] V. Yang, M. Groenert, G. Taraschi, C. Leitz, A. Pitera, M. Currie, Z. Cheng, and E. Fitzgerald, “Monolithic integration of III-V optical interconnects on Si using SiGe virtual substrates,” *Journal of Materials Science: Materials in Electronics*, vol. 13, no. 7, pp. 377–380, 2002.

[75] A. Pal, A. Nainani, Z. Ye, X. Bao, E. Sanchez, and K. Saraswat, “Electrical characterization of GaP-silicon interface for memory and transistor applications,” *IEEE Transactions on Electron Devices*, vol. 60, no. 7, pp. 2238–2245, 2013.

[76] H. Wagner, T. Ohrdes, A. Dastgheib-Shirazi, B. Puthen-Veettil, D. König, and P. P. Altermatt, “A numerical simulation study of gallium-phosphide/silicon heterojunction passivated emitter and rear solar cells,” *Journal of Applied Physics*, vol. 115, no. 4, p. 044508, 2014.

[77] J. Zhao, A. Wang, and M. A. Green, “24.5% efficiency silicon PERT cells on MCZ substrates and 24.7% efficiency PERL cells on FZ substrates,” *Progress in Photovoltaics: Research and Applications*, vol. 7, no. 6, pp. 471–474, 1999.

[78] K. M. Yu, W. Walukiewicz, J. W. Ager, III, D. Bour, R. Farshchi, O. D. Dubon, S. X. Li, I. D. Sharp, and E. E. Haller, "Multiband GaNAsP quaternary alloys," *Applied Physics Letters*, vol. 88, no. 9, p. 092110, 2006.

[79] R. Kudrawiec, A. V. Luce, M. Gladysiewicz, M. Ting, Y. J. Kuang, C. W. Tu, O. D. Dubon, K. M. Yu, and W. Walukiewicz, "Electronic band structure of GaNPAs highly mismatched alloys: Suitability for intermediate-band solar cells," *Physical Review Applied*, vol. 1, p. 034007, Apr 2014.

[80] A. Luque and A. Martí, "Increasing the efficiency of ideal solar cells by photon induced transitions at intermediate levels," *Physical Review Letters*, vol. 78, pp. 5014–5017, 1997.

[81] N. López, L. A. Reichertz, K. M. Yu, K. Campman, and W. Walukiewicz, "Engineering the electronic band structure for multiband solar cells," *Physical Review Letters*, vol. 106, p. 028701, 2011.

[82] T. Akatsu, C. Deguet, L. Sanchez, F. Allibert, D. Rouchon, T. Signamarcheix, C. Richtarch, A. Boussagol, V. Loup, F. Mazen, J.-M. Hartmann, Y. Campidelli, L. Clavelier, F. Letertre, N. Kernevez, and C. Mazure, "Germanium-on-insulator substrates—a novel engineered substrate for future high performance devices," *Materials Science in Semiconductor Processing*, vol. 9, no. 4–5, pp. 444 – 448, 2006.

[83] G. E. Cirlin, V. G. Dubrovskii, Y. B. Samsonenko, A. D. Bouravleuv, K. Durose, Y. Y. Proskuryakov, B. Mendes, L. Bowen, M. A. Kaliteevski, R. A. Abram, and D. Zeze, "Self-catalyzed, pure zincblende GaAs nanowires grown on Si(111) by molecular beam epitaxy," *Physical Review B*, vol. 82, p. 035302, 2010.

[84] P. D. Ye, G. D. Wilk, B. Yang, J. Kwo, S. N. G. Chu, S. Nakahara, H.-J. L. Gossmann, J. P. Mannaerts, M. Hong, K. K. Ng, and J. Bude, "GaAs metal–oxide–semiconductor field-effect transistor with nanometer-thin dielectric grown by atomic layer deposition," *Applied Physics Letters*, vol. 83, no. 1, pp. 180–182, 2003.

[85] S. Koveshnikov, W. Tsai, I. Ok, J. C. Lee, V. Torkanov, M. Yakimov, and S. Oktyabrsky, "Metal-oxide-semiconductor capacitors on GaAs with high-k gate oxide and amorphous silicon interface passivation layer," *Applied Physics Letters*, vol. 88, no. 2, p. 022106, 2006.

[86] W. P. Li, X. W. Wang, Y. X. Liu, S. I. Shim, and T. P. Ma, "Demonstration of unpinned GaAs surface and surface inversion with gate dielectric made of Si_3N_4," *Applied Physics Letters*, vol. 90, no. 19, p. 193503, 2007.

[87] M. Passlack, M. Hong, and J. P. Mannaerts, "Quasistatic and high frequency capacitance–voltage characterization of Ga_2O_3–GaAs structures fabricated by in situ molecular beam epitaxy," *Applied Physics Letters*, vol. 68, no. 8, pp. 1099–1101, 1996.

[88] M. Bosund, P. Mattila, A. Aierken, T. Hakkarainen, H. Koskenvaara, M. Sopanen, V.-M. Airaksinen, and H. Lipsanen, "GaAs surface passivation by plasma-enhanced atomic-layer-deposited aluminum nitride," *Applied Surface Science*, vol. 256, no. 24, pp. 7434 – 7437, 2010.

[89] M. Bosund, T. Sajavaara, M. Laitinen, T. Huhtio, M. Putkonen, V.-M. Airaksinen, and H. Lipsanen, “Properties of AlN grown by plasma enhanced atomic layer deposition,” *Applied Surface Science*, vol. 257, no. 17, pp. 7827 – 7830, 2011.

Aalto-DD 135/2014

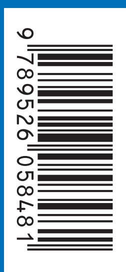

ISBN 978-952-60-5848-1
ISBN 978-952-60-5849-8 (pdf)
ISSN-L 1799-4934
ISSN 1799-4934
ISSN 1799-4942 (pdf)

Aalto University
School of Electrical Engineering
Department Micro- and Nanosciences
www.aalto.fi

BUSINESS +
ECONOMY

ART +
DESIGN +
ARCHITECTURE

SCIENCE +
TECHNOLOGY

CROSSOVER

DOCTORAL DISSERTATIONS